

# Diurnal variations of upper tropospheric and lower stratospheric winds over Japan as revealed with middle and upper atmosphere radar (34.85°N, 136.10°E) and five reanalysis data sets

T. Sakazaki,<sup>1</sup> M. Fujiwara,<sup>1</sup> and H. Hashiguchi<sup>2</sup>

Received 28 May 2010; revised 21 September 2010; accepted 1 October 2010; published 18 December 2010.

[1] Diurnal variations in the troposphere are a source of the diurnal tides which are the prevalent dynamical phenomenon in the mesosphere and lower thermosphere. They are also discussed as contributing to the excitation of Rossby waves. Here we study diurnal variations of upper tropospheric and lower stratospheric winds (up to 22 km) over Japan from 1986 to 2008 mainly using data from the middle and upper atmosphere (MU) radar (34.85°N, 136.10°E) and JRA25/JCDAS data, as well as other four global reanalysis data sets (ERA40, ERA-Interim, NCEP1, and NCEP2) and output data from Global Scale Wave Model (GSWM). The diurnal and semidiurnal components are extracted and analyzed. For the diurnal wind component, the MU radar data are used to validate the reanalysis data, and the reanalysis data are chosen for the analysis. The diurnal amplitude monotonically increases with height above 15–20 km. The diurnal phase shows an upward progression up to 15 to 20 km, while above 15 to 20 km, it shows a downward progression in most months. It is found that the diurnal tide, defined as the diurnal component with absolute zonal wave numbers of  $\leq 6$ , is dominant in the upper troposphere (explaining 60 to 80% of the variance) and in the stratosphere (explaining 80 to 90% of the variance). It is also observed that medium-scale waves contributed to the diurnal wind component in the upper troposphere from winter to spring ( $\sim 20\%$  of the variance). For the semidiurnal wind component, only MU radar data are used for the analysis, which confirmed that the semidiurnal migrating tide is dominant through the troposphere and the lower stratosphere. The semidiurnal tidal amplitude shows a marked seasonal variation in the troposphere; the amplitude is largest in winter ( $\sim 0.4 \text{ m s}^{-1}$ ) and smallest in summer ( $\sim 0.2 \text{ m s}^{-1}$ ).

**Citation:** Sakazaki, T., M. Fujiwara, and H. Hashiguchi (2010), Diurnal variations of upper tropospheric and lower stratospheric winds over Japan as revealed with middle and upper atmosphere radar (34.85°N, 136.10°E) and five reanalysis data sets, *J. Geophys. Res.*, 115, D24104, doi:10.1029/2010JD014550.

## 1. Introduction

[2] Diurnal variations in the troposphere and the stratosphere are important in several ways. First, they affect the upper atmosphere, second impact weather and climate, and finally, impact trend analysis, as described in the following paragraphs.

[3] First, in the upper atmosphere, atmospheric tides are the dominant phenomena. In this study, we follow the example of previous studies [e.g., Hagan *et al.*, 1995] and define the diurnal (semidiurnal) tide as the diurnal (semidiurnal) component with absolute zonal wave numbers of  $\leq 6$ . Tides are mainly excited in the troposphere and the stratosphere, and they partially travel into the upper atmosphere, with their amplitude increasing with height. The

main excitation sources for tides are considered to be radiative heating by tropospheric water vapor and stratospheric ozone [e.g., Chapman and Lindzen, 1970], in addition to latent heat release from deep convections in the tropics [e.g., Hagan and Forbes, 2002, 2003]. The tidal components are classified into two different components. The “migrating component” is defined as a Sun-synchronous, westward propagating wave, while all other components are termed “nonmigrating components.” Because heating is roughly zonally uniform, the migrating component is basically dominant. Nonmigrating components, which are generated mainly through zonally asymmetric heating and/or nonlinear interactions with tides and planetary waves, also have a particularly important role near the surface and in the upper atmosphere [e.g., Wallace and Tadd, 1974; Lieberman, 1991; Dai and Wang, 1999; Talaat and Lieberman, 1999; Huang and Reber, 2004; Forbes *et al.*, 2006; Oberheide *et al.*, 2006]. Importantly, tides (particularly nonmigrating components) observed in the mesosphere and the thermosphere are not fully reproduced by a tidal model [e.g., Forbes and Wu, 2006; Zhang *et al.*, 2006]. One of the reasons is that the

<sup>1</sup>Graduate School of Environmental Science, Hokkaido University, Sapporo, Japan.

<sup>2</sup>Research Institute for Sustainable Humanosphere, Kyoto University, Uji, Japan.

tropospheric forcing is not accurately parameterized. A quantitative investigation of tides in the excitation region (i.e., the troposphere and the stratosphere), including their excitation mechanisms, is therefore essential for studying tides.

[4] Second, diurnal variations may impact the weather and climate. Diurnal tides in the troposphere can contribute to cirrus cloud formation [Fujiwara *et al.*, 2009] and precipitation [Woolnough *et al.*, 2004] in the tropics. In addition, some of the diurnal variations in the midlatitude troposphere may contribute to the excitation of Rossby waves. Sato *et al.* [1993] discovered medium-scale waves in the upper troposphere, which propagated eastward with zonal wavelengths of 2000 to 3000 km, zonal phase speeds of 20 to 30 m s<sup>-1</sup>, and periodicities of ~24 h. These waves are interpreted as edge waves (Rossby waves), trapped at the tropopause in the baroclinic atmosphere [e.g., Eady, 1949; Tomikawa *et al.*, 2006]. Kodama *et al.* [2008] suggested that medium-scale waves over East Asia might be excited by diurnal wind systems over the Tibetan Plateau. Thus, in this case as well, diurnal variations in the troposphere might influence the climate system of the Earth because these waves contribute to the movements of upper clouds [Kodama *et al.*, 2008] and possibly to the mixing of substances across the midlatitude tropopause [Sato *et al.*, 2000].

[5] Finally, estimates of diurnal and subdiurnal variations are also essential for investigating climatological trends, because most of the upper air data are obtained from temporally coarse observations [e.g., Seidel *et al.*, 2005].

[6] Thus, a comprehensive understanding of diurnal variations in the tropopause and the stratosphere is important. However, as noted by Sakazaki and Fujiwara [2010a, 2010b] (hereafter referred to as SF10a and SF10b, respectively), there are relatively few previous studies on diurnal variations particularly below ~20 km in the midlatitudes; these studies are briefly summarized in the following paragraphs. This lack of reports is mainly because only a few subdiurnal upper air measurements have been conducted in the troposphere and the lower stratosphere.

[7] Previous studies that examined diurnal variations in the midlatitude troposphere and lower stratosphere were conducted mainly from the viewpoint of two types of diurnal variations, local wind systems and atmospheric tides. Most of these authors assumed that diurnal wind variations in the upper air (above 3 to 5 km) were caused only by the diurnal tide. For the diurnal component, Wallace and Hartranft [1969] and Wallace and Tadd [1974] examined diurnal wind variations up to 28 km (30 hPa) at locations all over the world, including midlatitude regions, by analyzing radiosonde data. The authors found that the diurnal wind component around this height has large nonmigrating tidal components, particularly in the troposphere. Subsequent studies using radiosonde data over Japan [Yoshida and Hirota, 1979] and over China [Huang *et al.*, 2009], and global analysis data [Hsu and Hoskins, 1989] showed similar results. In addition, these studies emphasized a strong seasonal dependence of the diurnal wind component (both amplitude and phase) particularly in the upper troposphere to lower stratosphere (~20 km). However, in these studies, the horizontal scale of the diurnal wind component was not estimated quantitatively. As a result, the contributions from migrating and nonmigrating components

were not estimated quantitatively. Furthermore, it is not clear if the diurnal tide is dominant at this height region.

[8] For the semidiurnal wind component, previous studies have found that the semidiurnal migrating tide is dominant in both the troposphere and the stratosphere, by analyzing radiosonde data [Wallace and Tadd, 1974] and atmospheric radar data [e.g., Whiteman and Bian, 1996]. In both cases, seasonal variations in semidiurnal amplitudes have yet to be examined.

[9] Two studies, SF10a and SF10b, recently investigated diurnal wind variations in the lower troposphere (below ~5 km) over Japan, predominantly using data from 31 stations of the wind profiler network in Japan (WINDAS) and from five analysis/reanalysis data sets. The authors found that the diurnal wind component was caused by at least four (not two) different phenomena: (1) local wind systems, (2) diurnal eastward moving eddies, which propagate eastward with a horizontal wavelength of ~1500 km and a zonal phase speed of 10 to 15 m s<sup>-1</sup>, (3) medium-scale waves, and (4) atmospheric tides. The former two wind systems were confined to the region below ~3 km, and the latter two wind systems were dominant above ~3 km. As for the diurnal eastward moving eddies (2 above), SF10b suggested that they were probably excited at mountainous regions and interpreted as the edge waves trapped at the lower boundary in the baroclinic atmosphere [Eady, 1949]. With regard to the semidiurnal wind component, SF10a confirmed the importance of the migrating tide above ~1 km. Below ~1 km, the semidiurnal wind component encompassed local wind systems and was examined by Sakazaki and Fujiwara [2008]. The SF10a and SF10b studies also found that the semidiurnal tidal amplitude was largest in winter (~0.4 m s<sup>-1</sup>) and smallest in summer (~0.2 m s<sup>-1</sup>) over the lower troposphere.

[10] As a follow-up study to SF10a and SF10b, the goal of the current study is to investigate the detailed characteristics of diurnal wind variations above ~5 km in the upper troposphere and the lower stratosphere over Japan, where the WINDAS network cannot make observations, using the MU (middle and upper atmospheric) radar. Data from the MU radar have been used in many previous studies to examine temporally small-scale phenomena, such as gravity waves and typhoons (see Fukao [2007] for a review).

[11] In the current study, all available horizontal wind data at 2 to 22 km from 1986 to 2007 were compiled to examine diurnal wind variations. In addition, we show that five different reanalysis data sets reproduce the diurnal wind component observed with the MU radar data reasonably well. These reanalysis data are chosen to examine the characteristics of the diurnal wind component in northern midlatitudes. The reanalysis data are utilized to decompose the observed diurnal component into each zonal wave number component, allowing to quantitatively estimate the contributions from the two dominant phenomena, the diurnal tide (both the migrating component and the nonmigrating components) and the medium-scale waves. Only the MU radar data are used for the analysis of the semidiurnal winds since they cannot be resolved by 6-hourly reanalysis data.

[12] The remainder of the manuscript is organized as follows. Section 2 describes the data sets and the analysis methods, while section 3 describes diurnal wind variations from the MU radar data. Section 4 examines the detailed

**Table 1.** Description of Five Reanalysis Data Sets

	JRA25	ERA-40	ERA-Interim	NCEP1	NCEP2
Horizontal resolution	$1.25^\circ \times 1.25^\circ$	$2.5^\circ \times 2.5^\circ$	$1.5^\circ \times 1.5^\circ$	$2.5^\circ \times 2.5^\circ$	$2.5^\circ \times 2.5^\circ$
Vertical levels	23	23	37	17	17
Period	1979 to present	1957–2002	1989 to present	1948 to present	1948 to present

characteristics of the diurnal wind component and the quantitative estimates of contributions from the diurnal tide and the medium-scale waves, which are determined using the reanalysis data. Section 5 details the semidiurnal wind component using MU radar data, and section 6 summarizes the main findings of this research.

## 2. Data and Analysis Methods

### 2.1. Data Description

[13] The MU radar, a MST radar operated by Research Institute for Sustainable Humanosphere (RISH) of Kyoto University is a 46.5 MHz pulse-modulated monostatic Doppler radar located at (34.85°N, 136.10°E; Shigaraki, Shiga, Japan). Details of the MU radar systems have been previously described by *Fukao et al.* [1985] and *Fukao* [2007]. Since 1986, the MU radar in the troposphere-stratosphere observation mode has been observing the upper air winds in the height range of 2 to 25 km with a vertical resolution of 150 m and a time resolution of 1 min. The minimum height of measurement (~2 km) is determined by the time needed to switch between transmission and reception. The maximum height (~25 km) is determined by the transmitting power and the antenna aperture. The beam direction is electrically changed to the vertical, northward, eastward, southward, and westward on a pulse-to-pulse basis using the active phased array method. The four oblique beams have zenith angles of 10°, allowing for horizontal wind measurements. In this study, the horizontal wind data ( $u$ : eastward wind,  $v$ : northward wind) from 2 to 22 km are used for analysis. Measurements were made on a campaign basis. One measurement campaign continued for about five days per month. We use data from 267 campaigns conducted from March 1986 to December 2007 (~1400 days in total).

[14] In addition to the MU radar data, we use the following five global reanalysis data sets to examine the global structures of diurnal wind variations: the NCEP/NCAR reanalysis data (NCEP1) [*Kalnay et al.*, 1996], the NCEP-DEO AMIP-II reanalysis data (NCEP2) [*Kanamitsu et al.*, 2002], two kinds of ECMWF reanalysis data (ERA40 and ERA-Interim) [*Uppala et al.*, 2002, 2008], and Japanese reanalysis data (JRA25/JCDAS; hereafter referred as JRA25) [*Onogi et al.*, 2007]. These data sets are all 4 times daily at 0000, 0600, 1200, and 1800 UTC. The periods of time that the data cover are different among the data sets, as shown in Table 1. The number of pressure levels for each data set is the following: 17 for NCEP1 and NCEP2, 23 for ERA40 and JRA25, and 37 for ERA-Interim, with top levels at 10 hPa for NCEP1 and NCEP2, 1 hPa for ERA40 and ERA-Interim, and 0.4 hPa for JRA25. It is important to note that the MU radar data are measured at height levels, while the reanalysis data are provided at pressure levels. In the

following analyses, we assume that the annual mean geopotential heights of reanalysis data correspond to the height levels of MU radar data, since the seasonal variation of geopotential height is negligible (<1 km) (not shown). We do not take into account the ground level of the MU radar station at 375 m; therefore, the “heights” mentioned in this paper are heights from this level. It should be noted that the MU radar observations are not assimilated in these reanalysis data.

[15] Additionally, output data from the Global Scale Wave Model (GSWM) [*Hagan et al.*, 1995, 1999; *Hagan and Forbes*, 2002, 2003] are compared with our results as a reference for atmospheric tides. The GSWM is a two-dimensional, linearized, steady state numerical tidal and planetary wave model that covers the region from the ground to the thermosphere. In this study, we analyze the diurnal and semidiurnal tides from two types of GSWM data sets, GSWM00 and GSWM02. The GSWM00 data set considers radiative heating with zonally uniform tropospheric water vapor and stratospheric ozone as excitation sources. The GSWM02 data set considers zonally uniform and asymmetric latent heat release with zonal wave numbers  $\leq 6$ , as well as the heating considered in GSWM00. As a result, the output data from GSWM00 includes only the migrating component, while that from GSWM02 includes both the migrating component and the nonmigrating components with absolute zonal wave numbers of  $\leq 6$ . Neither the topography nor the sensible heat flux in the boundary layer is considered by GSWM00 and GSWM02. The horizontal spacing of the output data is  $5^\circ \times 5^\circ$ , with a vertical resolution of 4 km. Previous studies analyzed and estimated the GSWM in the mesosphere-thermosphere altitudinal range at all latitudes [e.g., *Forbes and Wu*, 2006; *Forbes et al.*, 2006; *Zhang et al.*, 2006] and in the troposphere-stratosphere in the tropics [e.g., *Zeng et al.*, 2008]. However, to our knowledge, this analysis was not performed for the troposphere and the stratosphere at midlatitudes, except for *Huang et al.* [2009] and SF10b.

[16] Finally, radiosonde data collected at Yonago (35.4°N, 133.3°E) from 1992 to 1998 are used to obtain the climatological tropopause heights (Figures 6, 8–12, and 14). The tropopause is defined as the lowest level at which the lapse rate decreases to 2 K km<sup>-1</sup> or less, and the average lapse rate from this level to any level within the next higher 2 km does not exceed 2 K km<sup>-1</sup>.

### 2.2. Analysis Methods

[17] The MU radar data include a significant number of outliers, which probably result from both aircraft and ground clutter echoes. We remove such data through two screening processes and prepared hourly data sets with a vertical resolution of 1 km; the details are described in Appendix A.

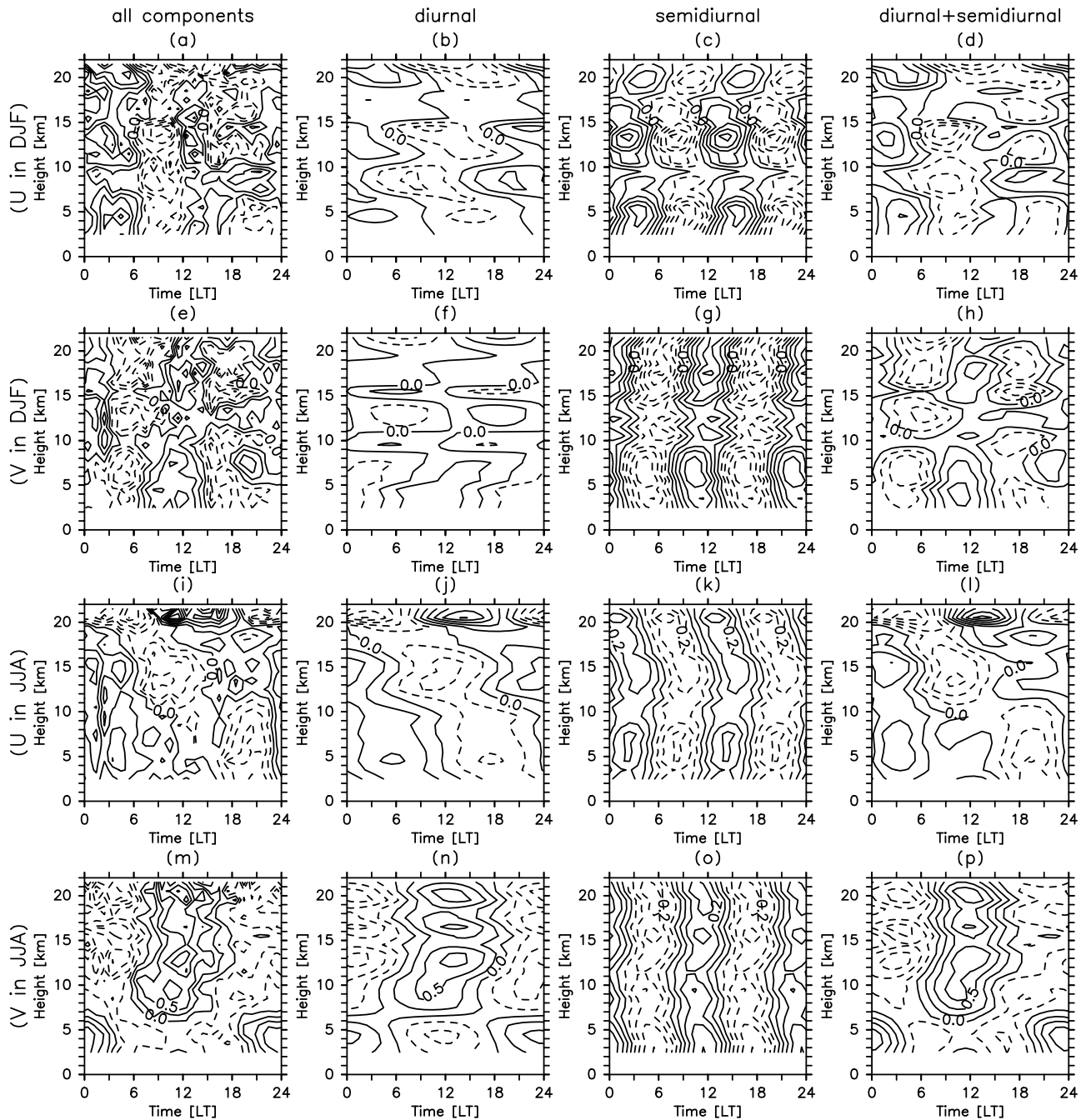


**Figure 1.** Time-height distributions of diurnal variations in (a–d) the zonal wind in December through February (DJF), (e–h) the meridional wind in DJF, (i–l) the zonal wind in June through August (JJA), and (m–p) the meridional wind in JJA, as derived from the MU radar data. Figures 1a, 1e, 1i, and 1m are for hourly anomaly variations including all components. Figures 1b, 1f, 1j, and 1n are for the diurnal component. Figures 1c, 1g, 1k, and 1o are for the semidiurnal component. Figures 1d, 1h, 1l, and 1p are for variations reconstructed from the diurnal and semidiurnal components only. The contour interval is  $0.1 \text{ m s}^{-1}$  for the semidiurnal wind (Figures 1c, 1g, 1k, and 1o) and  $0.25 \text{ m s}^{-1}$  for the others. The dotted lines show the westward and southward winds for  $u$  and  $v$ , respectively.

[18] The procedures employed in data processing and analysis for the hourly MU radar data and for the 6-hourly reanalysis data are basically the same as those used in SF10a and SF10b. However, they are briefly described below. The hourly (for MU radar data) and 6-hourly (for reanalysis data) local time composite horizontal winds ( $u$  and  $v$ ) are calculated for each height and for each month. For each monthly composite data set, three-monthly running mean is calculated to include the month before and after the month of interest (e.g., the composite data for January consists of December through February data).

[19] Using this data set, the 24 h mean wind and the hourly (for MU radar data) and 6-hourly (for reanalysis data) anomaly winds are calculated. Then, using a Fourier transformation, the diurnal and semidiurnal components (i.e., their amplitude and phase) are calculated for the MU radar data. For the reanalysis data, only the diurnal component is calculated because of the four-times daily resolution. Hereafter, the term “phase” refers to the local time when each component ( $u$  and  $v$ ) attains its maximum value. For the MU radar data, we follow the method explained by SF10a to calculate the standard errors of the amplitudes and the phases of the diurnal and semidiurnal components. Here, we assume that the deviation of each original hourly datum from the composite value is caused by random errors.

[20] For the reanalysis data, two kinds of composite data are calculated. One (denoted as R1; for example, JRA25-R1) is obtained using the data from the time and height when and where the MU radar data are present and judged as valid. For this data set, reanalysis data are interpolated to the MU radar height levels using the cubic spline method. The other type of composite data calculated (denoted as R2) is obtained using all of the data from 1990 to 2001. We select this period of time because it is covered by all of the reanalysis data sets. The R1 data set yields the most accurate comparison including data availability and sampling, and is used to validate the diurnal wind component calculated from the reanalysis data, presented below in section 4.1; the R2 data set is utilized to examine the characteristics of the diurnal wind component, discussed in sections 4.2 and 4.3.

[21] In addition, for the reanalysis data, we decompose the diurnal component into each zonal wave number  $s$ , as

$$X(\lambda, \phi, z, t) = \sum_{s=-n}^n [a_s(\phi, z) \cos(\omega t + s\lambda) + b_s(\phi, z) \sin(\omega t + s\lambda)], \quad (1)$$

following the method by *Haurwitz and Cowley* [1973]. Here,  $X$  is either  $u$  or  $v$ ;  $\lambda$ ,  $\phi$ , and  $z$  are longitude, latitude, and altitude, respectively;  $t$  is time in Universal Time (UT);  $n$  is half the total number of grid points in longitude;  $a_s$  and  $b_s$  are harmonic amplitudes, and  $\omega$  is the angular velocity of the Earth’s rotation, associated with the diurnal tide. The sign of  $s$  represents the direction of wave propagation, with positive values for westward propagating disturbances. The component  $s = 1$  represents the migrating component, and the others ( $s \neq 1$ ) represent nonmigrating components.

### 3. Diurnal Wind Variations

[22] We provide an overview of the diurnal wind variations observed with the MU radar. Figure 1 shows the time-height

distributions of hourly anomaly zonal and meridional winds in December, January, and February (DJF) and in June, July, and August (JJA). Figure 1 is calculated from the MU radar data. Figure 1 also depicts the diurnal and semidiurnal components, as extracted from the hourly anomaly winds, and the diurnal plus semidiurnal variations, which are reconstructed from only the diurnal and semidiurnal components. We see that these two components well reproduce the detailed features of the original variations. For the diurnal wind component, the amplitudes are  $\sim 0.5 \text{ m s}^{-1}$ , and the phases vary considerably with height, particularly in DJF. The phases differ greatly between DJF and JJA, suggesting a strong dependence on the season. In contrast, the semidiurnal wind component has a vertically standing structure for  $u$  and  $v$  and in both DJF and JJA, as is the case for the WINDAS results shown in SF10a. The phase of  $u$  ( $v$ ) is  $\sim 0300 \text{ LT}$  ( $\sim 0000 \text{ LT}$ ), and it has no variation with the season. However, the amplitudes are different between DJF and JJA. For example, the amplitude at 5 km is  $\sim 0.4 \text{ m s}^{-1}$  in DJF and  $\sim 0.3 \text{ m s}^{-1}$  in JJA (note that the contour interval is  $0.1 \text{ m s}^{-1}$  for only the semidiurnal component); these two components are discussed further in sections 4 and 5, respectively.

## 4. Results and Discussion: Diurnal Wind Component

[23] In this section, we examine the diurnal wind component. In section 4.1, we show that the reanalysis-R1 data reasonably reproduce the diurnal wind component calculated from the MU radar observation data. For section 4.2, the vertical structure and seasonal variation of the diurnal component are examined using the reanalysis-R2 data. In section 4.3, we further discuss the contributions from the diurnal tide and the medium-scale waves quantitatively using the reanalysis-R2 data.

### 4.1. Validation of Reanalysis Data

[24] Figures 2 and 3 show the vertical profiles of the diurnal amplitudes and phases for  $u$  and  $v$ , respectively, in DJF, March through May (MAM), JJA, and September through November (SON), as derived from the MU radar data and the JRA25-R1 data. For the MU radar data, two results are shown. One is from hourly sampled, hourly averaged data, and the other is from 6-hourly sampled, hourly averaged data. For the JRA25-R1 data, two results are also shown. The first is from 6-hourly sampled, original 6-hourly snapshot data, and the second is from hourly sampled, hourly interpolated data produced with the cubic spline method.

[25] These results demonstrate that for both the MU radar data and the JRA25-R1 data, the amplitudes and phases do not significantly depend on the difference in sampling interval (1 h or 6 h). The difference between the results from the different sampling intervals for most months and heights is within  $\pm 30\%$  for amplitude and within  $\pm \pi/4$  (rad) for phase.

[26] The comparison of the MU radar results with the JRA25-R1 results shows that the diurnal amplitudes and phases from the hourly sampled, hourly averaged MU radar data (black solid curves) are reproduced reasonably well by those from the 6-hourly sampled, 6-hourly snapshot JRA25-R1 data (red dashed curves), including their vertical

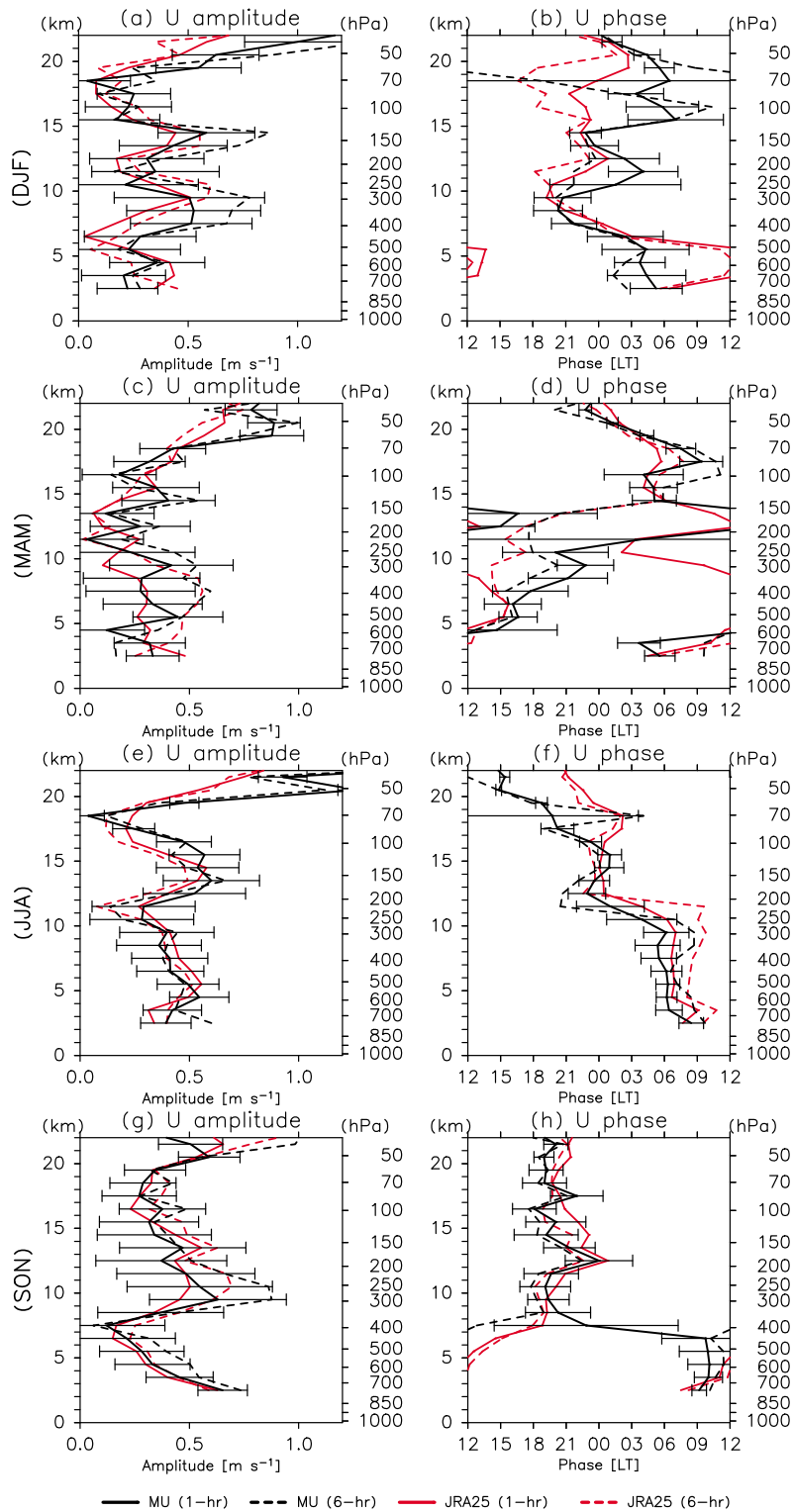


**Figure 2.** Vertical profiles of (a, c, e, and g) the amplitude and (b, d, f, and h) the phase of the diurnal zonal wind component in the following block of time: December through February (DJF) (Figures 2a and 2b), March through May (MAM) (Figures 2c and 2d), June through August (JJA) (Figures 2e and 2f), and September through November (SON) (Figures 2g and 2h). Black solid curves are obtained from the hourly sampled, hourly averaged MU radar data, and black dashed curves are from the 6-hourly sampled, hourly averaged MU radar data. Red solid curves are from the hourly sampled, hourly interpolated JRA25-R1 data, and red dashed curves are from the 6-hourly sampled, 6-hourly snapshot JRA25-R1 data. Horizontal bars represent standard errors. The reanalysis data are interpolated into MU radar height levels by the cubic spline method.

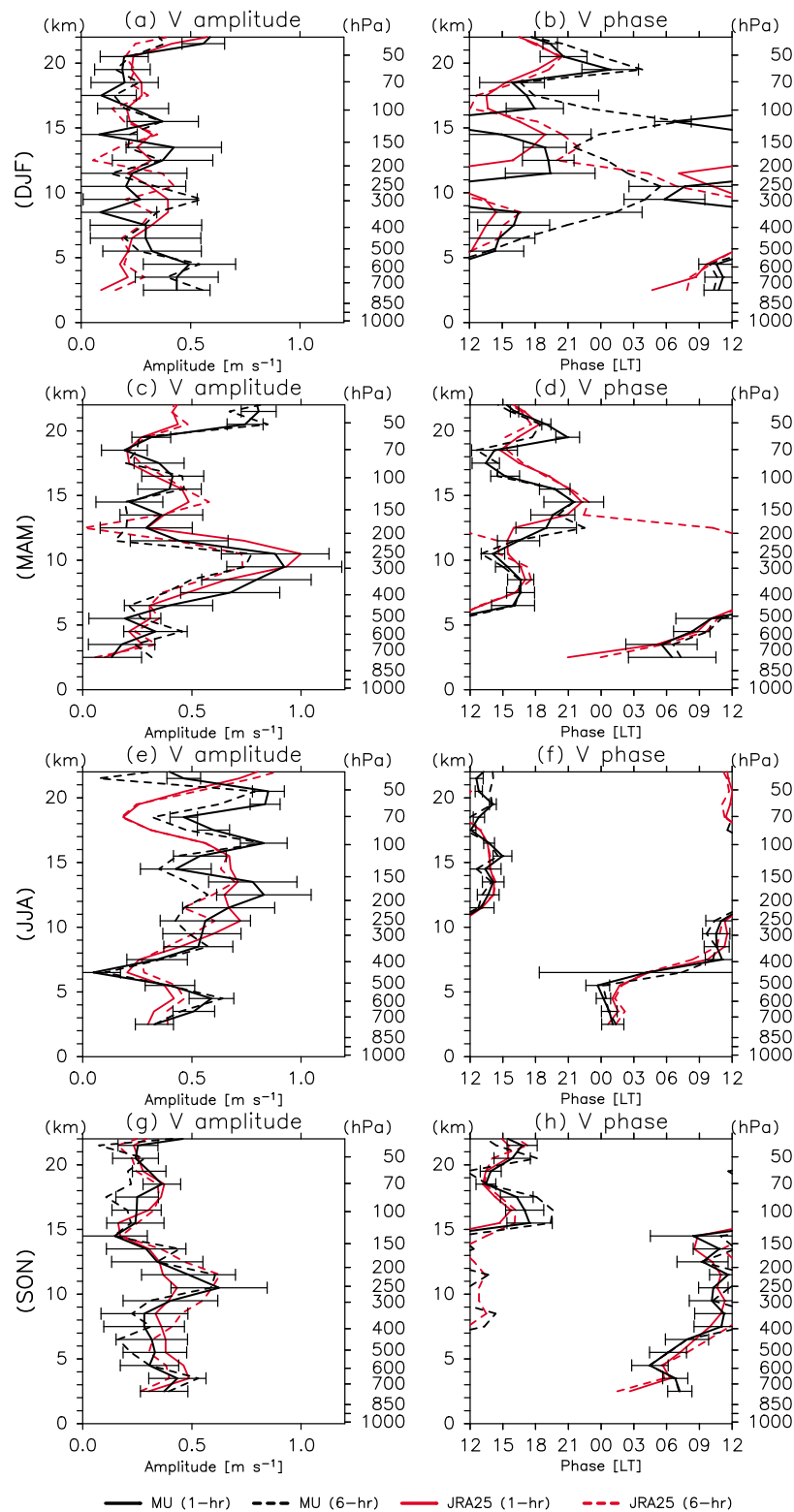
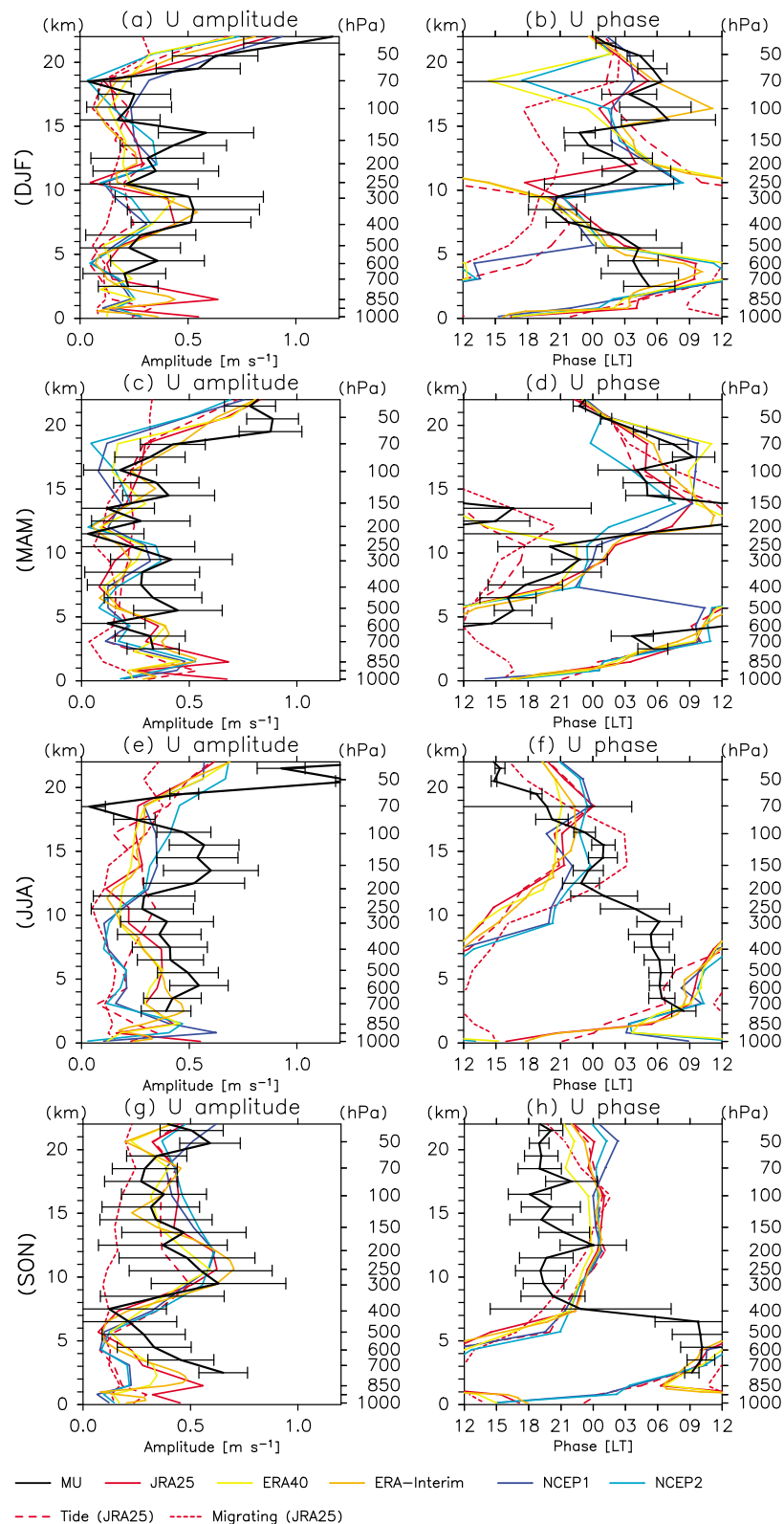


Figure 3. Same as for Figure 2 but for the diurnal meridional wind component.

structures and seasonal variations. For example, the large amplitudes for  $u$  and  $v$  above 15 to 20 km, along with those for  $v$  at 5 to 15 km in JJA and at  $\sim 10$  km in MAM, are apparent in both the MU radar data and the reanalysis data results; for the

phases, the curves from the two data sets almost overlap with each other except at some heights in DJF. Quantitatively, the differences in amplitudes and phases between the two results are within  $\pm 30\%$  and  $\pm \pi/4$  (rad), respectively, although in



**Figure 4.** Same as Figure 2, except the data are showing the diurnal zonal wind component from 6-hourly sampled, 6-hourly reanalysis-R2 data. Yellow lines represent the ERA40 data, and orange lines stand for the ERA-Interim data. Blue lines are for the NCEP1 data, and light blue lines are for the NCEP2 data. Red dashed lines stand for the diurnal tide defined as the components with absolute zonal wave numbers of  $\leq 6$  ( $|s| \leq 6$ ), as derived from the JRA25-R2 data. Red dotted lines are for the migrating component ( $s = 1$ ) from the JRA25-R2 data. See text for details.

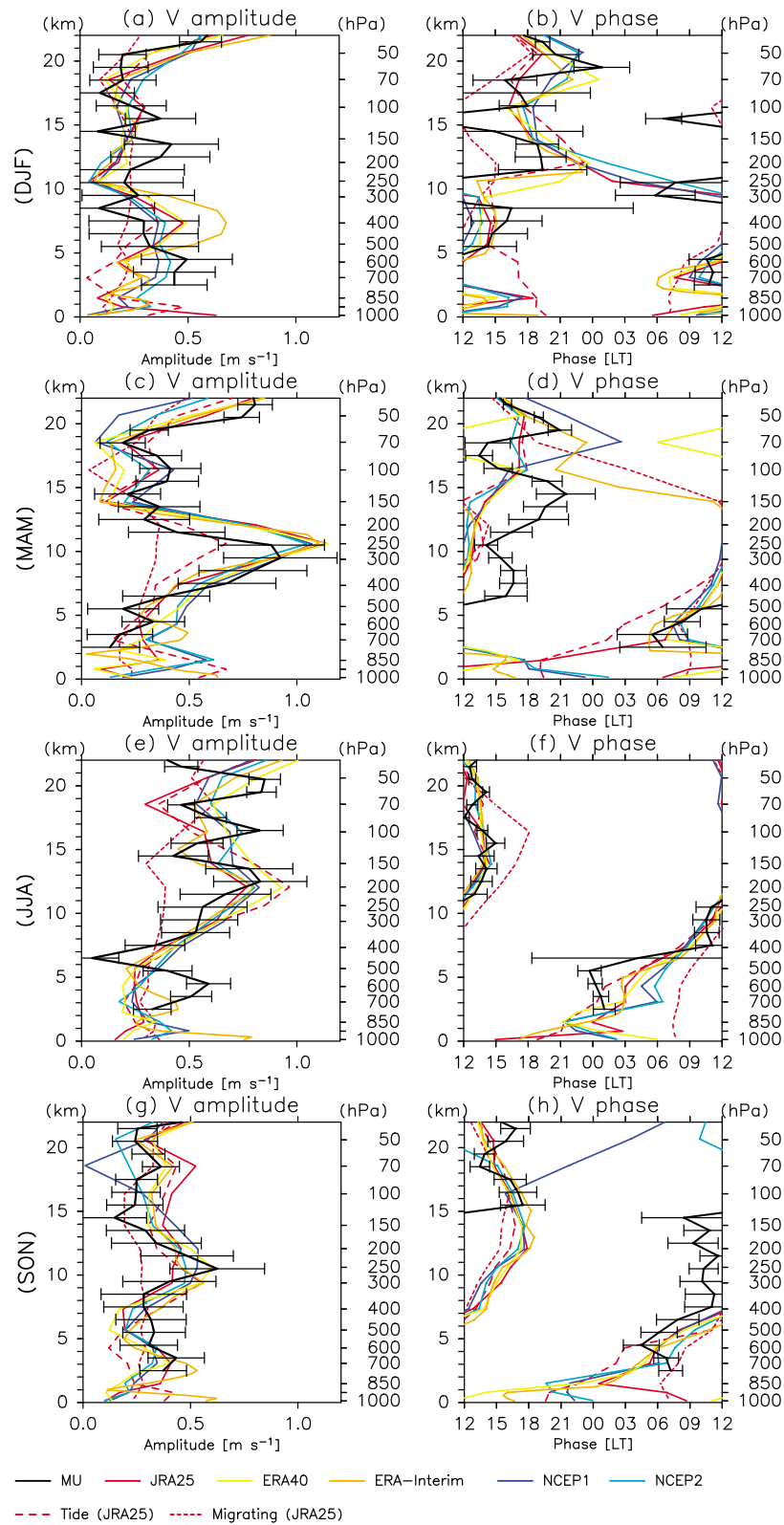


**Figure 5.** Same as Figure 4 but for the diurnal meridional wind component.

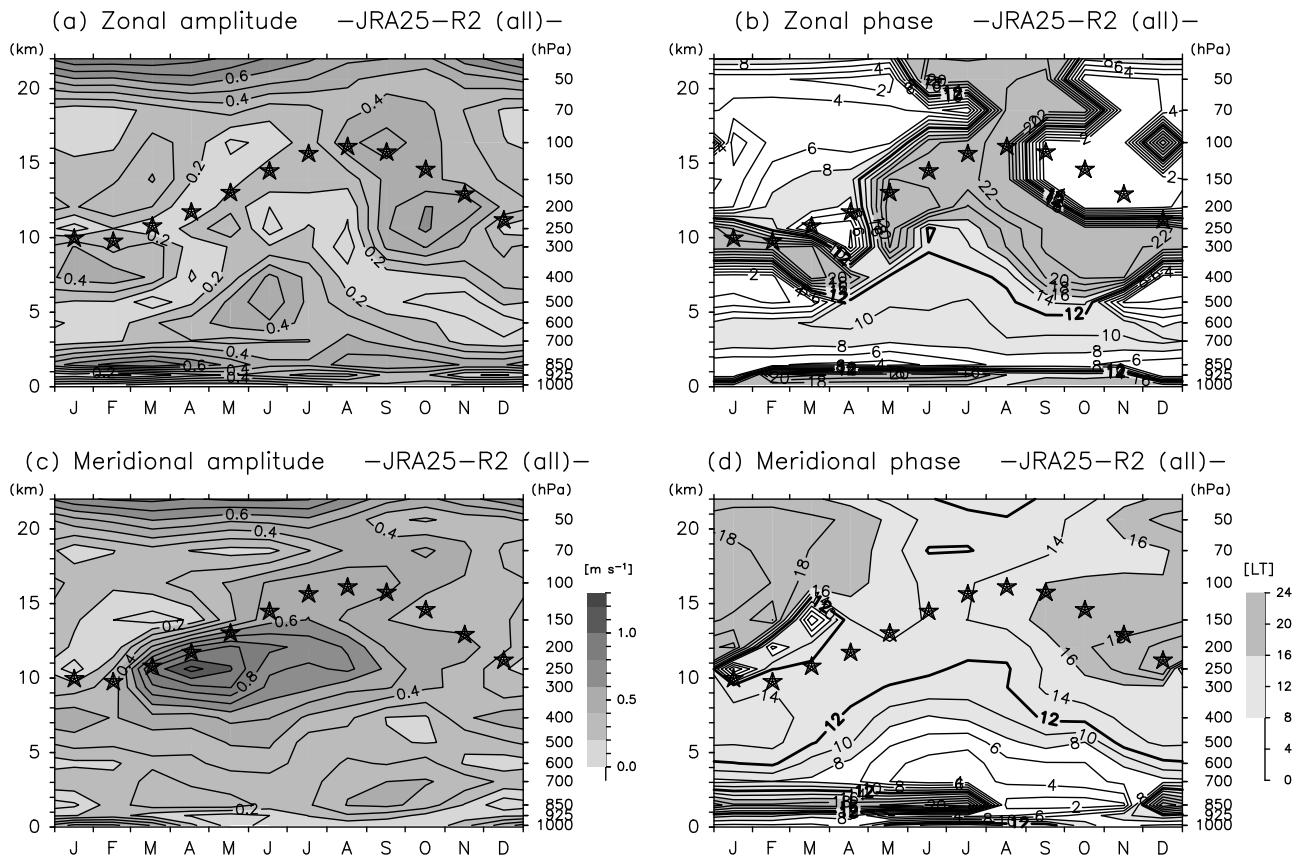


**Figure 6.** Month-height distributions of the following: (a) amplitude of  $u$ , (b) phase of  $u$ , (c) amplitude of  $v$ , and (d) phase of  $v$  for the diurnal component obtained from the JRA25-R2 data. Black stars represent the location of the tropopause at Yonago (35.4°N, 133.3°E), which are obtained from radiosonde data. The contour interval is 0.1  $\text{m s}^{-1}$  for Figures 6a and 6c, and 2 h for Figures 6b and 6d.

DJF they reach  $\sim \pm 50\%$  and  $\sim \pm \pi$  at some heights. Thus, it is concluded that the diurnal wind component in the MU radar data is reproduced reasonably well by the JRA25 data; that is, the JRA25 are validated at least in the troposphere and the lower stratosphere over Japan. The other four reanalysis data sets (ERA-Interim, ERA40, NCEP1, and NCEP2) show quantitatively similar results with respect to their sampling errors and ability to reproduce the results of the MU radar data (not shown).

[27] We have so far considered only the reanalysis data for the dates when also radar observations were taken (R1 data). Figures 4 and 5 show the vertical profiles of the diurnal amplitudes and phases for  $u$  and  $v$ , respectively, for each season, as derived from the full reanalysis data (R2 data). It is seen that the differences among the five reanalysis-R2 data sets are negligible. The profiles from the MU radar data (the same as in Figures 2 and 3) determine if the number of data points from the MU radar data used for the composite data is enough to obtain statistical characteristics. There are differences between the results from the MU radar data and those from the reanalysis data in Figures 4 and 5; for example, the zonal phases in JJA and SON are 3–6 h different, and the zonal amplitudes in JJA are  $\sim 0.3 \text{ m s}^{-1}$  smaller in the results from reanalysis data than those from the MU radar data. The difference might be partly because the number of data used for a composite data set is smaller for the MU radar data (200 to 300 days for a 1 month data set;

see Figure A2) than for the reanalysis-R2 data ( $\sim 1,100$  days for a 1 month data set), and partly because the composite from MU radar data are affected by short-time (10–20 days) variability of diurnal variations, which cannot be captured by MU radar observations (5 days per month). In section 4.2, the diurnal wind component from the reanalysis-R2 data is examined.

#### 4.2. Characteristics of Diurnal Wind Component

[28] In this section, we examine the results from the JRA25-R2 data. The other four reanalysis data sets give similar results (not shown). Figure 6 shows the month-height distributions of the diurnal amplitude from the 6-hourly sampled, 6-hourly snapshot JRA25-R2 data. The characteristics at 850 hPa are roughly consistent with those reported by SF10a in that the amplitude is large in spring and autumn.

[29] There is a remarkable change in the characteristics of the amplitudes and their altitude dependence around 20 km height. Below heights of 15 to 20 km, the amplitudes of  $u$  and  $v$  are 0.1 to 0.5  $\text{m s}^{-1}$  and 0.2 to 1.0  $\text{m s}^{-1}$ , respectively, throughout the year. The amplitude of  $v$  is basically larger than that of  $u$ . In addition, there is a marked seasonal variation for the amplitude of  $v$  below 20 km; it is relatively large (0.4 to 0.7  $\text{m s}^{-1}$ ) at 5 to 20 km in summer and attains its maximum value around the tropopause in spring ( $\sim 1.0 \text{ m s}^{-1}$ ). In contrast, above 15 to 20 km, the amplitudes for both  $u$  and  $v$  rapidly and monotonically increase with height, reaching

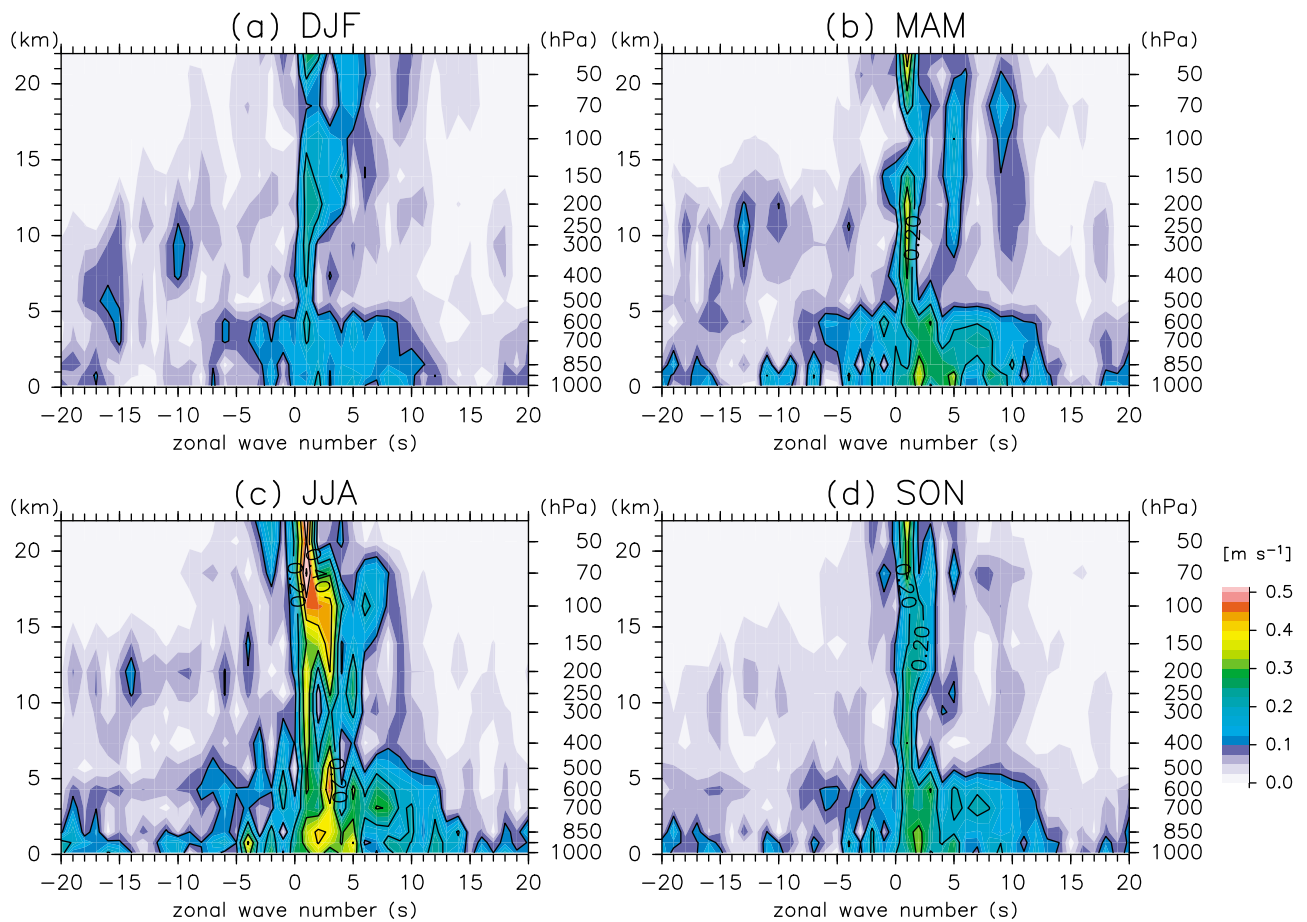


**Figure 7.** Zonal wave number-height distributions of the amplitude of the diurnal component of  $v$  at  $35^\circ\text{N}$ , as derived from the JRA25-R2 data. The contour interval is  $0.2 \text{ m s}^{-1}$ .

$0.5$  to  $1.0 \text{ m s}^{-1}$  at  $22 \text{ km}$  in most months (see also Figures 4 and 5).

[30] Figure 6 also shows month-height distributions of the diurnal phase obtained from the 6-hourly snapshot JRA25-R2 data. The observed phase characteristics below  $\sim 5 \text{ km}$  are consistent with those presented in SF10a. In DJF, the phase of  $u$  shows large variability below  $20 \text{ km}$ . Above this level, the phase decreases with height consistent with downward phase velocity (see also Figure 4b). In MAM, JJA, and SON, the phases of  $u$  show upward progressions up to the tropopause ( $\sim 12 \text{ km}$  in MAM,  $\sim 16 \text{ km}$  in JJA, and  $\sim 15 \text{ km}$  in SON); above these levels, they show downward progressions (see also Figures 4d, 4f and 4h). The height above which the phase propagates downward ( $15$  to  $20 \text{ km}$ ) roughly corresponds to the height above which the amplitudes monotonically increase with height ( $15$  to  $20 \text{ km}$ ). The phase structure of  $v$  is similar to that of  $u$ , except that the former precedes the latter by a quadrature. In addition, the phase also shows marked seasonal variation ( $3$  to  $12 \text{ h}$ ), particularly below  $\sim 20 \text{ km}$ . In DJF, the phase of  $u$  ( $v$ ) is  $\sim 0000 \text{ LT}$  ( $\sim 1400 \text{ LT}$ ) at  $5$  to  $10 \text{ km}$  and  $\sim 0300 \text{ LT}$  ( $\sim 1800 \text{ LT}$ ) at  $10$  to  $20 \text{ km}$ . In JJA, in contrast, the phase of  $u$  ( $v$ ) is  $1000$  to  $1800 \text{ LT}$  ( $0600$  to  $1200 \text{ LT}$ ) at  $5$  to  $10 \text{ km}$  and  $2000$  to  $2200 \text{ LT}$  ( $1200$  to  $1400 \text{ LT}$ ) at  $10$  to  $20 \text{ km}$ .

[31] Figure 7 shows the diurnal amplitudes of  $v$  for each zonal wave number ( $s$ ) and for each pressure level at  $35^\circ\text{N}$

for each season, as derived from the JRA25-R2 data. The  $u$  has similar results except that the amplitudes are generally smaller than  $v$ . It is seen in Figure 7 that the amplitudes of  $v$  are generally largest in JJA and smallest in DJF. This finding suggests that diurnal variability is strongest in JJA at this latitude. Large amplitudes are confined to the tidal components (i.e.,  $-6 \leq s \leq 6$ ), particularly above  $\sim 5 \text{ km}$ . Additionally, above  $\sim 5 \text{ km}$ , the migrating component has the largest amplitude at most heights, while nonmigrating components also have large amplitudes, particularly in JJA (e.g.,  $s = 3, 5$  and  $9$ ). The dominance of  $s = 5$ , and  $9$  is consistent with the findings by Tokioka and Yagai [1987], who suggested that they are excited by the heating related with the land-sea distributions in the tropics with zonal wave numbers of  $4$  and  $8$ . These nonmigrating components (particularly  $s = 3$ , and  $5$ ) are further discussed in section 4.3.1. In DJF and MAM, the components with  $-20 < s < -10$  also have relatively large amplitudes around the tropopause ( $\sim 10 \text{ km}$ ).

### 4.3. Mechanism of Diurnal Component

[32] In sections 4.3.1 and 4.3.2 we discuss in detail the contributions of the diurnal tide (section 4.3.1) and the medium-scale waves (section 4.3.2) to the total diurnal variations. Possible excitation mechanisms of diurnal tide are also discussed.

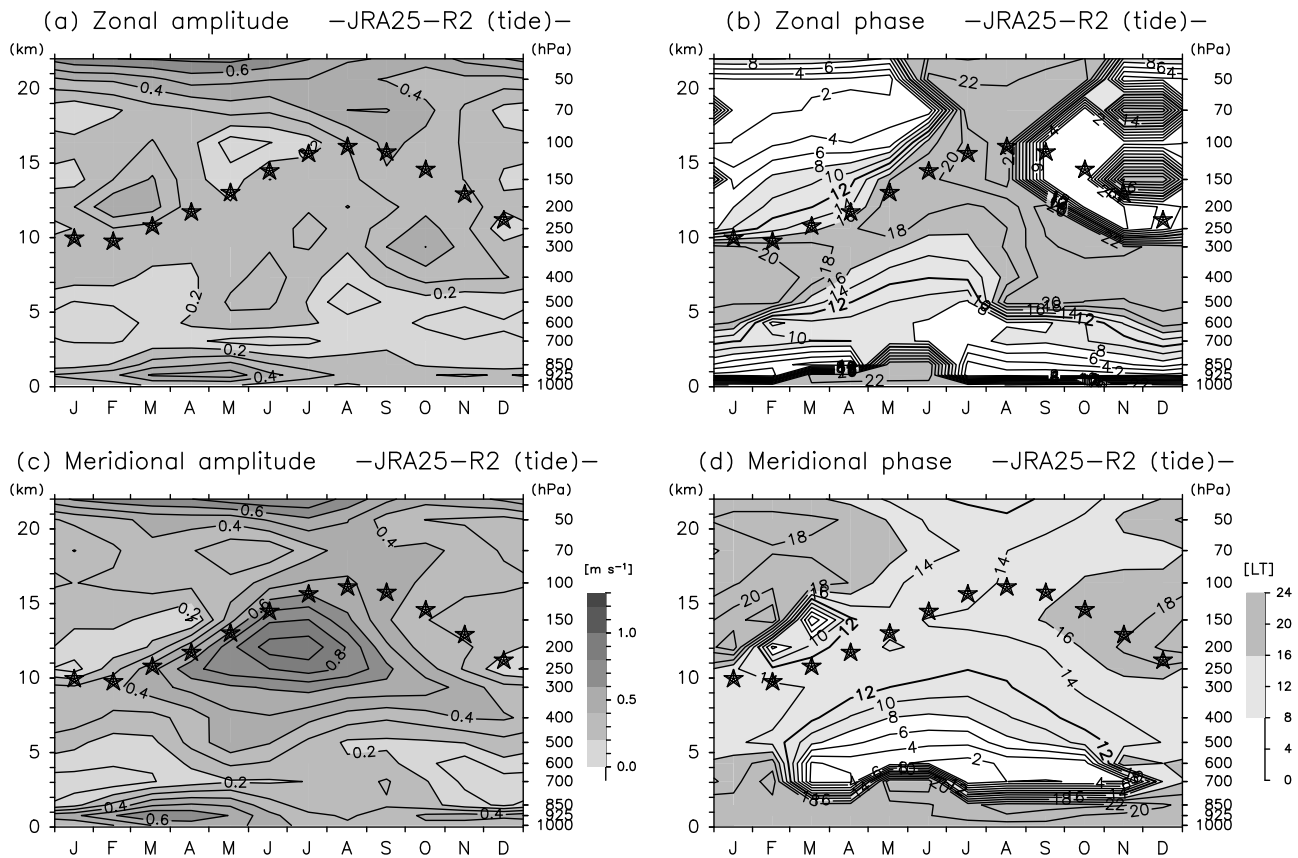


**Figure 8.** Same as Figure 6, except these data are showing the diurnal tide defined as the components with absolute zonal wave numbers of  $\leq 6$  ( $|s| \leq 6$ ), as obtained from the JRA25-R2 data.

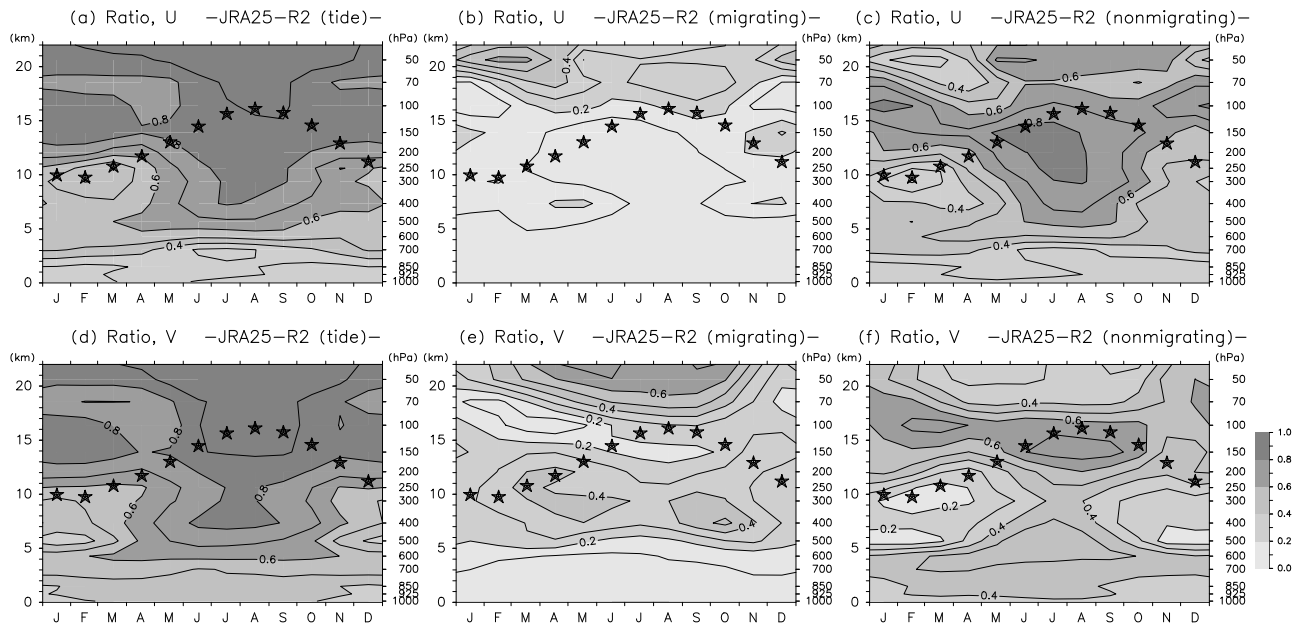


**Figure 9.** Month-height distributions of the ratios of (a, d) the diurnal tide, (b, e) the migrating component, and (c, f) the nonmigrating components to the total variance with all zonal wave number components, for  $u$  (Figures 9a, 9b, and 9c) and  $v$  (Figures 9d, 9e, and 9f), as derived from the JRA25-R2 data. Black stars represent the location of the tropopause at Yonago ( $35.4^\circ\text{N}$ ,  $133.3^\circ\text{E}$ ), which are obtained from radiosonde data. The contour interval is 0.1.

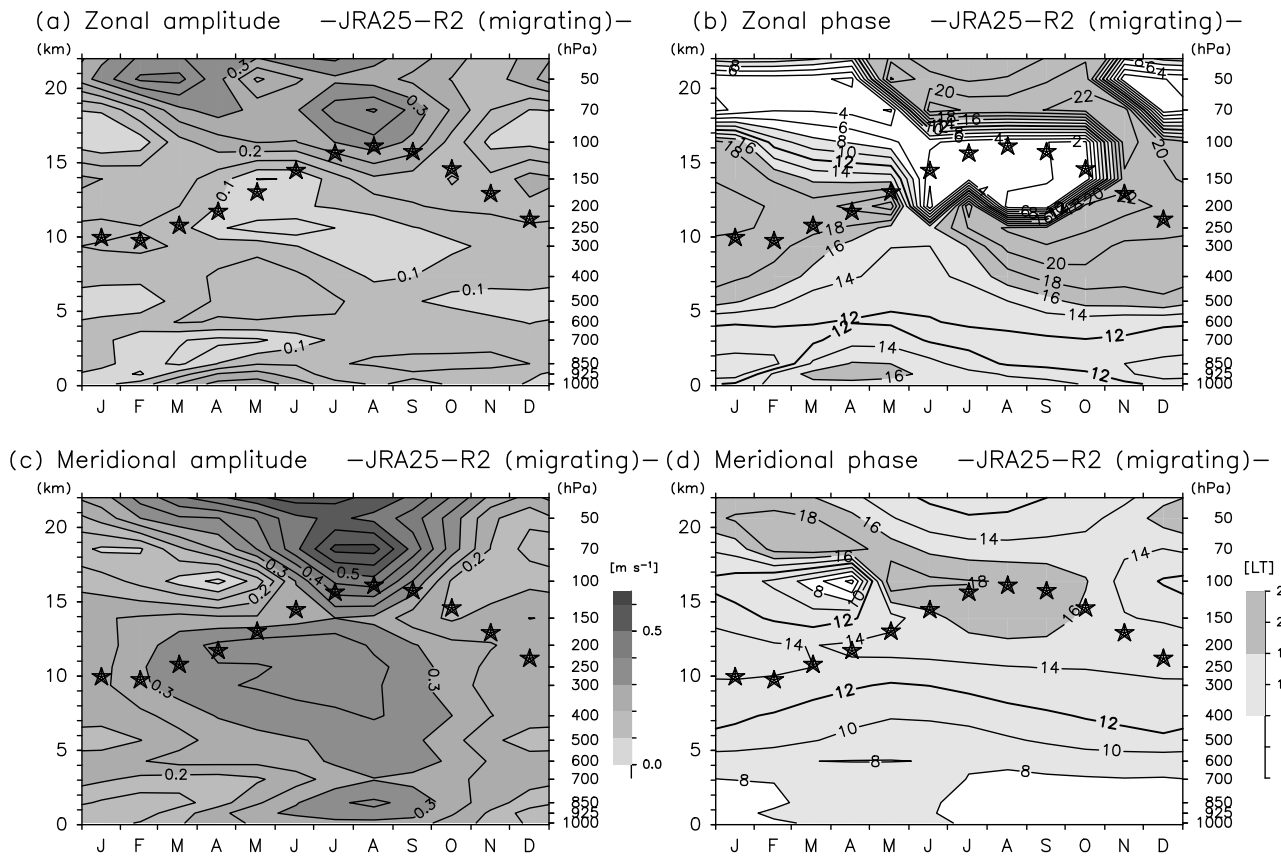


**Figure 10.** Same as Figure 6, except that the data represent the diurnal migrating component ( $s = 1$ ) from the JRA25-R2 data. The contour interval is  $0.05 \text{ m s}^{-1}$  for Figures 10a and 10c. The color contrast for the amplitude (Figures 10a and 10c) is different from Figures 6 and 8.

#### 4.3.1. Diurnal Tide

[33] As seen in Figure 7, the tidal amplitudes in most months are relatively large in the upper troposphere and the lower stratosphere. Figure 8 shows the month-height distributions of the diurnal tidal ( $|s| \leq 6$ ) amplitudes and phases calculated from the JRA25-R2 data. The amplitudes of  $u$  and  $v$  at 5 to 15 km are  $0.2$  to  $0.4 \text{ m s}^{-1}$  and  $0.2$  to  $0.9 \text{ m s}^{-1}$ , respectively. The amplitude of  $v$  at 5 to 15 km is largest in summer ( $\sim 0.9 \text{ m s}^{-1}$ ), while that of  $u$  shows no marked seasonal variation. Above 15 to 20 km, the amplitudes of  $u$  and  $v$  monotonically increase with height, reaching  $0.5$  to  $1.0 \text{ m s}^{-1}$  at 22 km. The phase of  $u$  ( $v$ ) shows an upward progression in the troposphere, reaching 2000 to 2400 LT (1400 to 1800 LT) at an area around the tropopause (10 to 20 km). In the lower stratosphere, the phase of  $u$  and  $v$  shows a downward progression. Additionally, the phase shows a marked seasonal variation, particularly below  $\sim 20$  km. The vertical wavelengths are large in JJA and SON (20 to 30 km), while they are smaller in DJF and MAM ( $\sim 10$  km). Figures 4 and 5 contain the detailed profiles (red dashed curves). This seasonal change in vertical wavelength is consistent with that reported by Huang *et al.* [2009] over China ( $118^\circ\text{E}$ ,  $31^\circ\text{N}$ ).

[34] Amplitudes and phases of the diurnal tides are largely consistent with the total diurnal variations shown in Figure 6, indicating that the diurnal tide largely controls the diurnal variations in the upper troposphere and the lower stratosphere. That is, the observed seasonal variations of the diurnal wind component in Figure 6 are largely due to the

seasonal changes in the diurnal tide. Figures 9a and 9d show the ratio of the tidal components ( $-6 \leq s \leq 6$ ) to the total variance (with all  $s$ ). The ratio is  $\sim 0.3$  ( $\sim 0.6$ ) at 5 km,  $\sim 0.6$  ( $\sim 0.8$ ) at 10 km, and  $\sim 0.8$  (0.8 to 0.9) at 15 to 22 km in DJF (JJA); the ratio increases with height. Note that the large amplitude of  $v$  around the tropopause in spring (March to May) is not seen in the tidal amplitude in Figure 8 (see also Figure 5c), and the ratio of tidal components are small around the tropopause from winter to spring (Figures 9a and 9d). These findings are confirmed to be due to the contribution from medium-scale waves in the section 4.3.2.

[35] As pointed out in section 4.2, the migrating component ( $s = 1$ ) is basically dominant in the upper troposphere and the lower stratosphere (Figure 7). Figure 10 shows the month-height distributions of the amplitude and the phase of the migrating component for  $u$  and  $v$ . Below 15 to 20 km, the amplitudes of  $u$  and  $v$  are  $0.1$  to  $0.2 \text{ m s}^{-1}$  and  $0.1$  to  $0.4 \text{ m s}^{-1}$ , respectively. The amplitude of  $v$  is two or three times larger than that of  $u$ . Additionally, the amplitude of  $v$  at 5 to 15 km is greatest in summer ( $0.3$  to  $0.4 \text{ m s}^{-1}$ ) and smallest in winter ( $\sim 0.2 \text{ m s}^{-1}$ ). Above 15 to 20 km, the amplitude monotonically increases with height, reaching  $0.2$  to  $0.4 \text{ m s}^{-1}$  and  $0.2$  to  $0.6 \text{ m s}^{-1}$  at 22 km for  $u$  and  $v$ , respectively. At this height, the amplitude is also largest in summer ( $\sim 0.4 \text{ m s}^{-1}$  for  $u$  and  $\sim 0.6 \text{ m s}^{-1}$  for  $v$ ) and smallest in the winter ( $\sim 0.2 \text{ m s}^{-1}$  both for  $u$  and  $v$ ). The phase profile of the migrating tide basically matches that of a tide with  $-6 \leq s \leq 6$ ; this observation is also seen in Figures 4 and 5, which

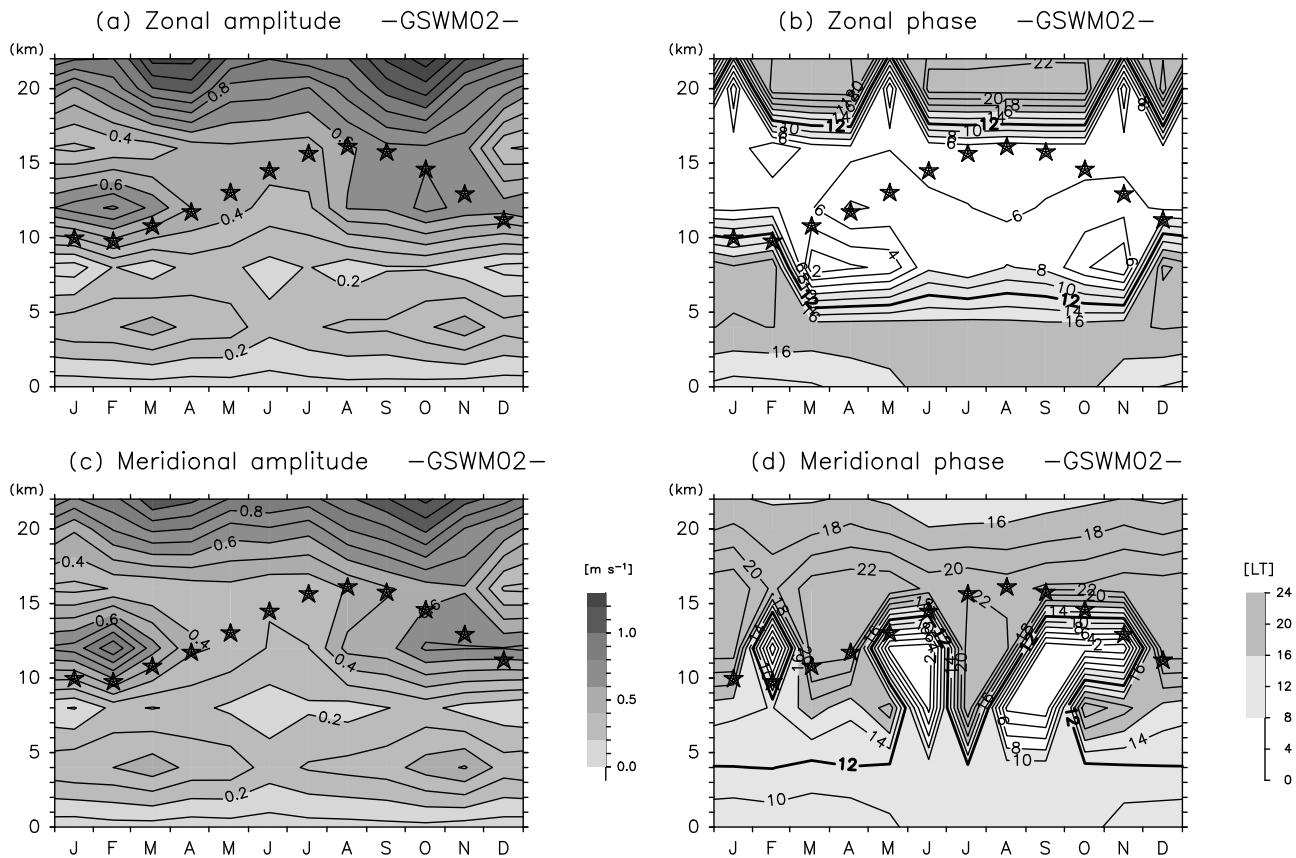


**Figure 11.** Same as Figure 6, except these data are showing the diurnal tide, as obtained from the GSWM02 data.

show the profiles relating to the migrating diurnal tide from the JRA25-R2 data (red dotted curves). However, the seasonal variation of the phase of the migrating tide is relatively weak, which indicates that the seasonal variation of the nonmigrating components largely contribute to that of the diurnal tide seen in Figure 8. The vertical wavelengths of the migrating component are estimated to be large in JJA and SON (20 to 30 km) and small in DJF and MAM ( $\sim 10$  km).

[36] Figure 9 also shows the ratios of the variance of the migrating component and nonmigrating components. At 5 to 15 km, the ratio of the migrating component for  $u$  ( $v$ ) is  $< 0.2$  (0.2 to 0.4), while that of the nonmigrating components for  $u$  ( $v$ ) is 0.4 to 0.8 (0.4 to 0.6), showing a non-negligible contribution. In fact, the large tidal amplitudes of  $v$  at 5 to 15 km in summer ( $\sim 0.8 \text{ m s}^{-1}$ ) are largely ( $\sim 60\%$ ) due to nonmigrating components. In contrast, above 15 km, the ratio of the migrating component increases with height, reaching  $\sim 0.4$  ( $\sim 0.6$ ) for  $u$  ( $v$ ) at 22 km. Thus, the diurnal tide above 15 to 20 km is largely (40 to 60%) caused by the migrating component, while that below 15 to 20 km is largely (40 to 80%) affected by nonmigrating components. These nonmigrating components cause large amplitudes of  $v$  in summer and a marked seasonal variation in phase below 15 to 20 km.

[37] We examine possible excitation sources of the diurnal tide in northern midlatitudes by comparing the diurnal tide in the JRA25-R2 data with that in the GSWM00 and

GSWM02 data sets. Figure 11 shows the month-height distributions of the diurnal tidal amplitudes and phases from GSWM02 data. Latent heat release is considered only in GSWM02 (section 2.1). In GSWM02 (GSWM00; results are not shown), the amplitudes of both  $u$  and  $v$  are  $0.1$  to  $0.6 \text{ m s}^{-1}$  ( $0.1$  to  $0.5 \text{ m s}^{-1}$ ) below 15 to 20 km; above 15 to 20 km, they rapidly and monotonically increase with height, reaching  $\sim 1.0 \text{ m s}^{-1}$  ( $0.5 \text{ m s}^{-1}$ ) at 22 km. The GSWM02 amplitudes are approximately twice the GSWM00 amplitudes, indicating the importance of excitation due to latent heat release. The vertical structures of the diurnal tidal amplitudes and phases in the GSWM02 and GSWM00 data are roughly consistent with those of the diurnal tide results from the reanalysis-R2 data. Specifically, the amplitude increases above 15 to 20 km, and there was a positive (negative) phase slope below (above) 15 to 20 km. Thus, the observed diurnal tide would be primarily excited by radiative heating of tropospheric water vapor and latent heat release below 15 to 20 km. The tidal phase profiles in Figures 8 and 10 suggest that, in the excitation height region at 5 to 15 km, both of the vertically propagating modes and vertically trapped modes of the diurnal tide are excited, causing interference with each other. Above this height range, only propagating modes exist, and the waves are freely propagating upward, which results in downward phase progression and increasing amplitudes. Considering that excitation sources are roughly confined to the area below the tropopause, the above sug-

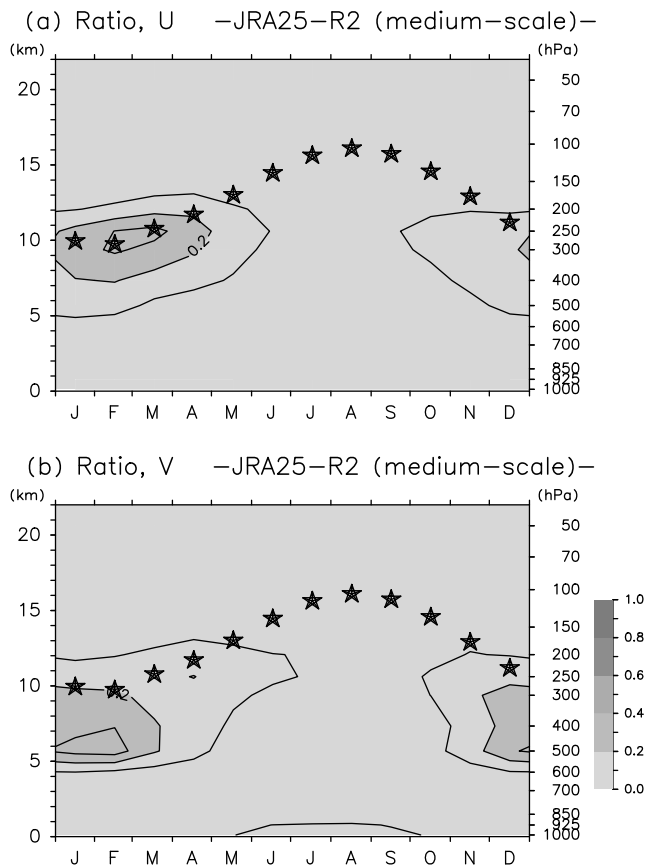


**Figure 12.** Same as Figure 9, except the data are showing the components with  $-20 \leq s \leq -10$ .

gestion is also supported by the finding that the height above which the phase shows a downward phase progression (i.e., the waves start to freely propagate upward) oscillates throughout the year in accordance with the seasonal variation of the tropopause height ( $\sim 10$  km in DJF-MAM and  $\sim 15$  km in JJA-SON) (Figures 8c, 8d, 10c and 10d).

[38] Differences between the diurnal tides calculated from the reanalysis-R2 data and those from the GSWM also exist. First, the amplitudes of  $u$  and  $v$  from the reanalysis-R2 data are smaller than those from GSWM02 at 15 to 22 km in MAM and SON (Figures 8 and 11). This difference is due to the fact that the amplitudes in the troposphere and stratosphere from the GSWM02 show a marked semiannual variation with a maximum in spring and autumn and a minimum in summer and winter (Figure 11). This semiannual variation may be related to the weak excitation of antisymmetric modes in GSWM02 reported by Zeng *et al.* [2008]. Second, the large tidal amplitudes of  $v$  in summer and the seasonal variation in phase at 5 to 15 km (particularly in JJA-SON), which are largely caused by nonmigrating components as shown above, are not consistent with the results from GSWM02 (see Figure 11). Also, the phase from the GSWM02 results shows no marked seasonal variation. For nonmigrating components, Tokioka and Yagai [1987] have theoretically shown that the diurnal forcing with a zonal wave number of  $k$  generates two diurnal non-

migrating tidal components,  $s = 1 + k$  and  $s = 1 - k$ . The authors also showed that the land-sea distribution in the tropics is roughly represented by  $k = 4$ , resulting in components with  $s = 5$  and  $s = -3$ . Latent heat releases in the tropics, which are influenced by land-sea distributions, also have similar wave number distributions [Williams and Avery, 1996; Forbes *et al.*, 1997]. In Figure 7, it is shown that the large nonmigrating components at 5 to 15 km in summer are caused by the components with  $s = 3, 5$ ; the latter is explained by the heat in the tropics, but the former is not. In this case, the relatively small amplitude of  $s = -3$ , compared with  $s = 5$ , might have been related to the efficiency of the tidal excitation; that is, if the depth of heating is  $h$ , then the mode with a vertical wavelength of  $2h$  will be most efficiently excited [Salby and Garcia, 1987]. In classical tidal theory, the vertical wavelengths of the first symmetric vertically propagating mode of the components with  $s = -3$  and  $s = 5$  are  $\sim 57$  km and  $\sim 20$  km, respectively [Williams and Avery, 1996]; the latter may be more efficiently excited by tropospheric heating with a vertical scale of 10 to 20 km. With regard to the large amplitude observed for  $s = 3$ , it may have been excited by heating that was not considered in the GSWM02. For example, the land-sea distribution in the northern midlatitudes is roughly represented by  $k = 2$  [e.g., Held, 1983]; the heating related to this topography generates the components  $s = 3$  and  $s = -1$ . In fact, latent heat release in the midlatitudes (not that in the tropics) has been shown to have similar wave number distributions [Forbes *et al.*, 1997, Figure 2]. In this case as well, the small amplitudes of the observed tidal winds for  $s = -1$ , compared with those for  $s = 3$ , may be due to the difference in vertical propagation. That is, in classical tidal theory, the first symmetric mode with a positive equivalent depth is a vertical propagating mode with a vertical wavelength of  $\sim 24$  km for  $s = 3$  while it is a vertically trapped mode (equivalent depth is 17.3 km) for  $s = -1$ .

#### 4.3.2. Medium-Scale Waves

[39] In this section, we discuss the large diurnal amplitude of  $v$  around the tropopause in winter and spring, which cannot be explained by the diurnal tide. Both SF10a and SF10b have found that the diurnal wind component in the upper troposphere is primarily controlled by medium-scale waves. In this study, analysis of the JRA25-R2 data shows that medium-scale waves with a zonal phase speed of  $\sim 25$  m  $s^{-1}$  and a zonal wavelength of 2000 to 3000 km are dominant around the tropopause in winter and spring (not shown). The amplitude is 0.5 to 1.0 m  $s^{-1}$  in the upper troposphere.

[40] As pointed out in section 4.2 and shown in Figure 7, the amplitudes of components with  $-20 \leq s \leq -10$  (eastward traveling components with a zonal wavelength of 1500–3000 km), which correspond to medium-scale waves, are relatively large around the tropopause, particularly in MAM. Figure 12 shows the ratio of the variance of the components with  $-20 \leq s \leq -10$  to the total variance. The ratio is relatively large (0.2 to 0.3) in the upper troposphere from winter to spring for both  $u$  and  $v$ , indicating a nonnegligible contribution to diurnal variability in the upper troposphere. These large ratios of medium-scale waves compensate for the small ratios of the diurnal tide at these heights in these months (Figures 9a and 9d). Thus, the maximum amplitude

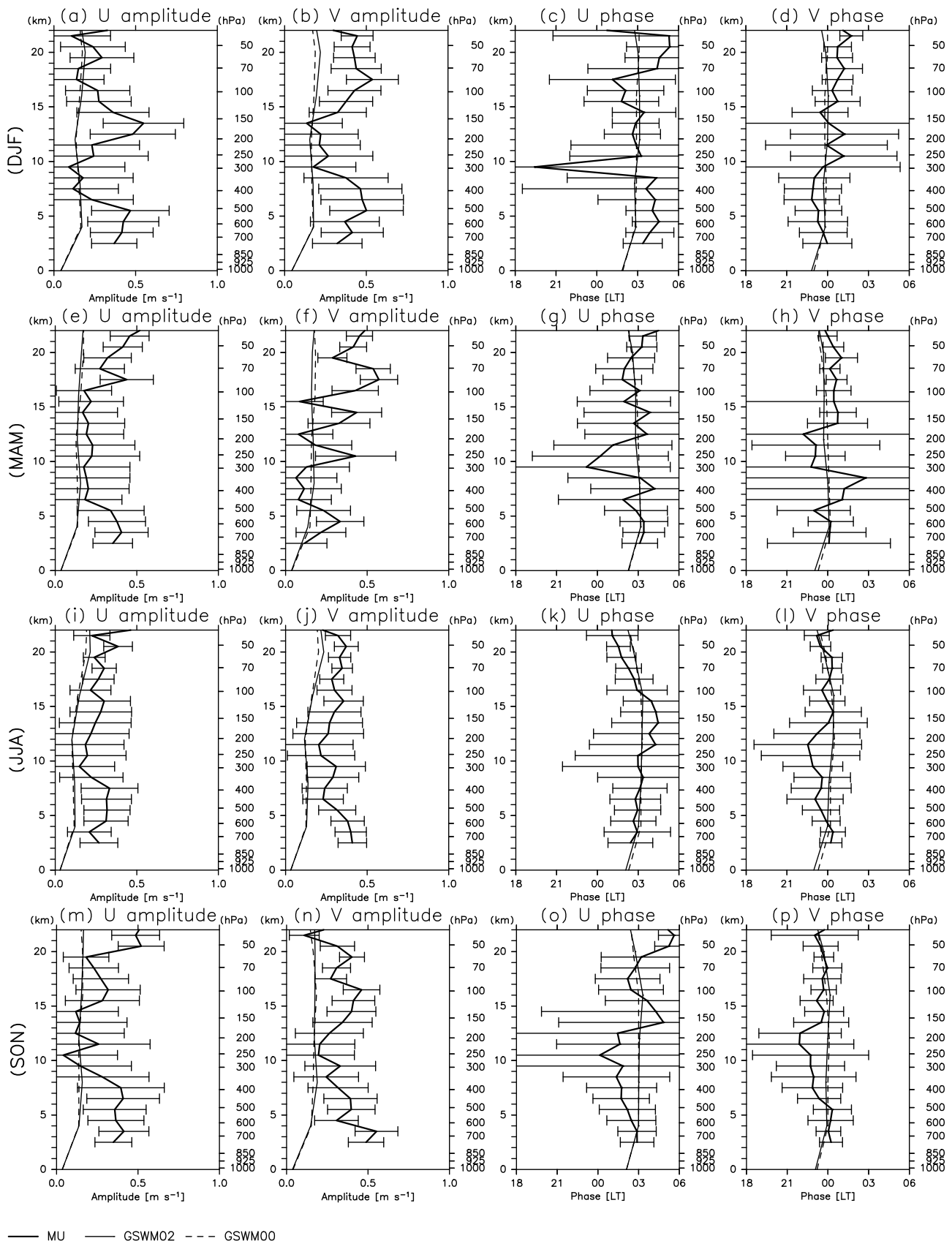


**Figure 13.** Same as Figure 4 but showing the semidiurnal wind component of both of  $u$  and  $v$ . Only the profiles from the MU radar data (thick solid lines), the GSWM02 (thin solid lines), and the GSWM00 (thin dashed lines) data are shown.

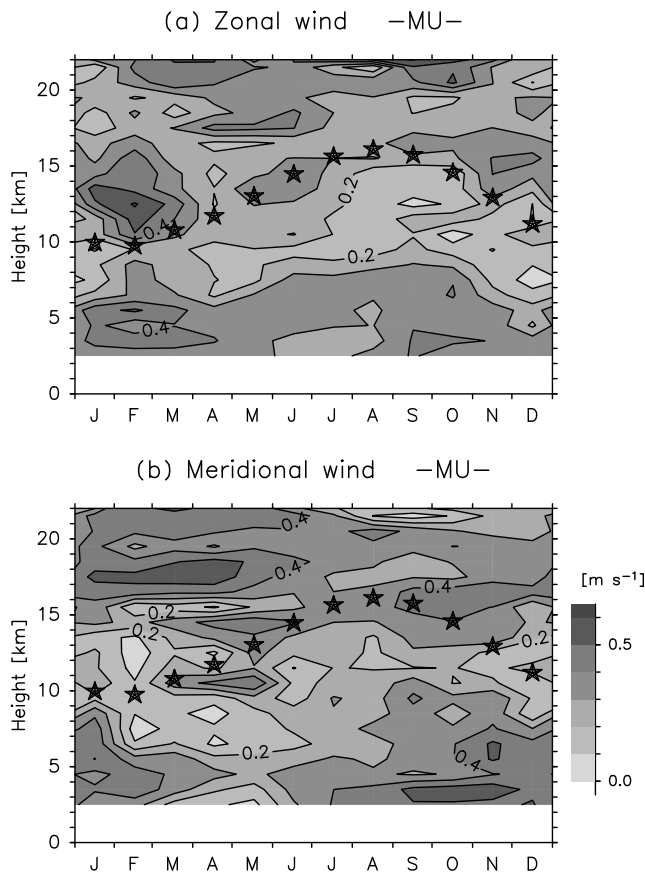


**Figure 14.** Same as Figures 6a and 6c but for the semidiurnal wind component from MU radar data.

for  $v$  around the tropopause in winter and spring are caused by superposition of the medium-scale waves on the diurnal tide.

## 5. Results and Discussion: Semidiurnal Component

[41] In this section, we present an investigation of the semidiurnal wind component. Because the semidiurnal component cannot be fully analyzed in 6-hourly reanalysis data, we examine only that from the MU radar data. Figure 13 shows the vertical profiles of the amplitudes and the phases of the semidiurnal wind component. The amplitude is 0.1 to 0.5  $\text{m s}^{-1}$  for both  $u$  and  $v$  throughout the year. Figure 14 shows the month-height distributions of the semidiurnal amplitudes for  $u$  and  $v$ . Although the standard errors are large ( $\sim 0.2 \text{ m s}^{-1}$ ) as seen in Figure 13, the amplitudes below the tropopause ( $\sim 10 \text{ km}$ ) are large in SON and DJF ( $\sim 0.4 \text{ m s}^{-1}$ ), and they are small in MAM and JJA ( $\sim 0.2 \text{ m s}^{-1}$ ). The characteristics of this seasonal variation are basically consistent with the finding reported by SF10a and SF10b for the lower tropospheric semidiurnal wind component (a maximum of  $\sim 0.4 \text{ m s}^{-1}$  in winter and a minimum of  $\sim 0.2 \text{ m s}^{-1}$  in the summer). In contrast, there seems no marked seasonal variation above  $\sim 10 \text{ km}$ . Both the GSWM00 and GSWM02 results also show a marked seasonal variation in amplitude in the troposphere. The GSWM00 and GSWM02 amplitudes at 3 to 12 km have a maximum of  $\sim 0.16 \text{ m s}^{-1}$  in

winter and a minimum of  $\sim 0.13 \text{ m s}^{-1}$  in summer (not shown), although they are significantly smaller than those from the MU radar (Figure 13). It was also reported that the semidiurnal pressure tide had its smallest amplitude in JJA in analyses of surface pressure data from observations [Dai and Wang, 1999] and reanalysis [Ray and Ponte, 2003].

[42] In Figure 13, the phase of  $u$  ( $v$ ) is nearly constant as  $\sim 0300 \text{ LT}$  ( $\sim 0000 \text{ LT}$ ) regardless of height, indicating that  $v$  precedes  $u$  by a quadrature. In addition, there is little seasonal variation in phase, unlike the diurnal wind component. These phases are basically consistent with those of the semidiurnal migrating wind component in tidal theory [Chapman and Lindzen, 1970; see also Whiteman and Bian, 1996] and the calculations from the GSWM00 and GSWM02 data (Figure 13). GSWM00 considers only the migrating component (section 2.1). Additionally, the observed phase profile is consistent with that of a semidiurnal migrating tide that has a principal mode (first symmetric propagating mode) with a very long vertical wavelength of  $\sim 200 \text{ km}$  [Chapman and Lindzen, 1970] which is excited through deep radiative heating by stratospheric ozone. Therefore, we conclude that the semidiurnal wind component is primarily controlled by the principal mode of the semidiurnal migrating tide throughout the troposphere and the lower stratosphere over Japan.

[43] It should be noted that if a principal mode of the migrating component only exists, the seasonal characteristics are expected to be similar over the entire troposphere and stratosphere because of its long vertical wavelength. However, as mentioned above, the observed seasonal characteristics in Figure 14 seem different between the troposphere and the stratosphere. Modes other than the principal mode of the migrating tide (i.e., higher-order symmetric modes of the migrating component, antisymmetric modes of migrating component, and nonmigrating components), which all have relatively smaller vertical wavelengths, may also make a contribution to the semidiurnal tide, particularly in the troposphere; this may affect on the marked seasonal variation in the troposphere. One possible excitation source for these modes with small vertical wavelengths is tropospheric heating (radiative heating and/or latent heat release), which has a typical vertical scale of 10 to 20 km. This heating efficiently excites modes with a vertical wavelength of 20 to 40 km.

## 6. Concluding Remarks

[44] We investigated diurnal wind variations in the upper troposphere and the lower stratosphere in midlatitudes over Japan using the MU radar data and five reanalysis data sets from 1986 to 2007. The diurnal and semidiurnal harmonic components were extracted from the local time composite of the horizontal wind data and were analyzed. For the diurnal wind component, the MU radar data were used for validating the reanalysis data, and these reanalysis data (JRA25 data) were then predominantly examined. For the semidiurnal wind component, which cannot be observed with reanalysis data, the MU radar data were examined.

[45] For the diurnal wind component, the amplitude is 0.1 to 1.0  $\text{m s}^{-1}$  below 15 to 20 km, while the amplitude of  $v$  is basically larger than that of  $u$ . Above 15 to 20 km, these amplitudes monotonically increase with height. In addition,

the amplitude of  $v$  has a maximum value at 5 to 20 km in summer (0.4 to 0.6 m s<sup>-1</sup>) and at ~10 km in spring (0.8 to 1.0 m s<sup>-1</sup>). The diurnal phase shows an upward progression to the tropopause and a downward progression in the stratosphere. Additionally, the phase shows a marked seasonal variation, particularly below ~20 km.

[46] Using reanalysis data, we decomposed the observed diurnal component into each zonal wave number component and quantitatively estimated the contribution from the diurnal tide (migrating/nonmigrating components) and from the medium-scale waves. All of the above characteristics, except for the large amplitudes of  $v$  at the tropopause in spring, are found to be controlled by diurnal tides with absolute zonal wave numbers of  $\leq 6$ . The contribution of the diurnal tide is 60 to 80% (of the variance) in the upper troposphere and 80 to 90% in the lower stratosphere. Of the tidal components, the migrating component is dominant (40–60% of the variance) above 15 to 20 km, while the nonmigrating components also make a significant contribution (40 to 80 % of the variance) below 15 to 20 km. In fact, both the large amplitudes of  $v$  at 5 to 15 km in summer and the seasonal variation in phase below ~20 km are largely caused by nonmigrating components.

[47] We also analyzed the diurnal tide in the troposphere and the lower stratosphere in midlatitudes, which was calculated from GSWM data (GSWM00 and GSWM02). The vertical structure is roughly consistent with that of the reanalysis data, suggesting that the observed diurnal tide is primarily excited by tropospheric water vapor and latent heat release in the tropics. However, differences from reanalysis data results also exist; these suggests that seasonal variations may not be complete in GSWM, and other heat sources that are not considered in GSWM, such as latent heat release in the midlatitudes, might contribute significantly to the diurnal tide in this height region.

[48] The large amplitudes of  $v$  in winter and spring in the upper troposphere are largely caused by medium-scale waves, which travel eastward with a zonal wavelength of 3000 km and a zonal phase speed of ~30 m s<sup>-1</sup>. These waves also contribute to the diurnal variability in these seasons at these heights (~20% of the variance).

[49] For the semidiurnal wind component, we confirmed that the semidiurnal migrating tide (the principal mode (first symmetric propagating mode) with a very long vertical wavelength) is predominant in the upper troposphere and the lower stratosphere. In addition, we observed that the semidiurnal tidal amplitude in the troposphere are largest in winter (~0.4 m s<sup>-1</sup>) and smallest in summer (~0.2 m s<sup>-1</sup>). These results suggest that modes other than the principal mode of the migrating tide, which might possibly excited by tropospheric heating, might influence the semidiurnal tide in the troposphere.

[50] We propose that reanalysis data can be used for the study of diurnal variations in the upper troposphere and the lower stratosphere. For the diurnal wind component, using reanalysis data, we were able to quantitatively estimate the horizontal scale and the contribution from each zonal wave number component. That is, the contributions from the migrating component and the nonmigrating components were for the first time quantitatively estimated in the troposphere and the lower stratosphere, where the diurnal tide is excited. In contrast, the semidiurnal component can only

be observed with high time resolution measurements such as the MU radar. Analysis of data from other radars at various locations is needed to reveal the global structure and the seasonal variation of the semidiurnal tide in the troposphere and the stratosphere. Also, it would be worthwhile that future reanalysis data have a finer temporal resolution (e.g., 1 h).

## Appendix A

[51] From the original MU radar data with a time resolution of 1 min and a vertical resolution of 150 m, we removed outlier data that was probably due to aircraft echoes and ground clutter echoes. We then produced hourly data with a vertical resolution of 1 km through two processes. The first process is based on the assumption that vertical winds are horizontally uniform over an area with a zenith angle of  $\leq 10^\circ$  (Appendix A1); the second process used reanalysis data to determine any outliers (Appendix A2).

### A1. First Process

[52] The MU radar uses five beams to calculate three wind components. Aircrafts are small compared with the area where the radar beams swing with a zenith angle of  $10^\circ$  (~9.5 km<sup>2</sup> at 10 km height). Additionally, the area of the beam itself (~0.31 km<sup>2</sup> at 10 km height; determined by the beam width of  $3.6^\circ$ ) is much smaller than the distance between two different beams (>1.7 km at 10 km height; determined by the zenith angle). Thus, aircrafts influence only one of the five beams at a particular time. For example, we consider a case where aircrafts might influence the oblique beam to the east. Doppler velocities along the beams to the east ( $V_{rE}$ ) and west ( $V_{rW}$ ) are represented as,

$$V_{rE} = w \cos \theta + u \sin \theta, \quad (\text{A1})$$

$$V_{rW} = w \cos \theta - u \sin \theta. \quad (\text{A2})$$

We define  $W_{diff}$  as the difference between the vertical wind estimated from the two oblique beams to the west and the east, and the vertical wind estimated from the vertical beam ( $w^*$ );

$$W_{diff} = \frac{V_{rE} + V_{rW}}{2 \cos \theta} - w^*. \quad (\text{A3})$$

In the case being considered, because aircraft velocities ( $u$  in  $V_{rE}$ ) are much faster than wind velocities ( $u$  in  $V_{rW}$ ),  $W_{diff}$  has large absolute values. In this study, we use 1 min MU radar data with a vertical resolution of 150 m only when the condition that  $|W_{diff}| < 1.0$  (m s<sup>-1</sup>) was satisfied. Similarly,  $W_{diff}$  for screening of meridional winds is defined as

$$W_{diff} = \frac{V_{rN} + V_{rS}}{2 \cos \theta} - w^*, \quad (\text{A4})$$

where  $V_{rN}$  and  $V_{rS}$  are the velocities along the oblique beams to the north and south, respectively.

### A2. Second Process

[53] Using the MU radar data remaining after the first screening process, we produced an hourly data set with a

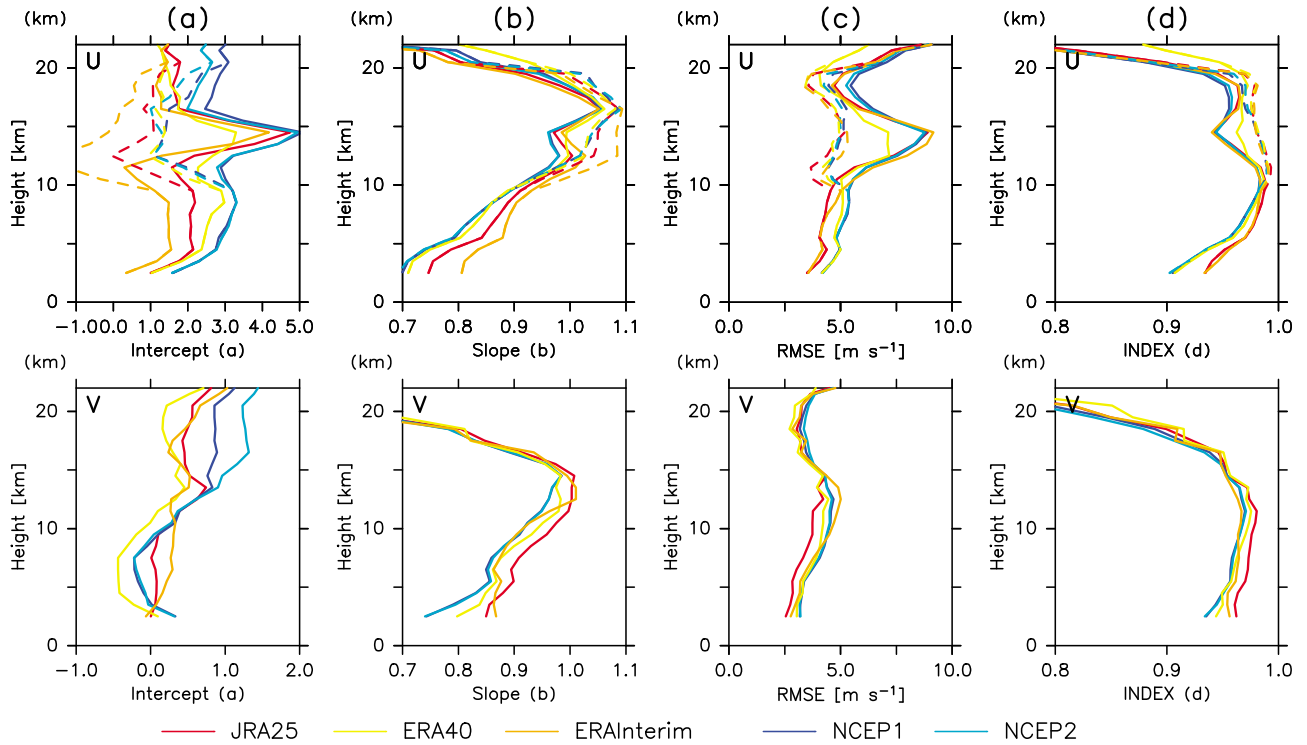


**Figure A1.** The comparison between the MU radar data and the reanalysis data. The vertical profiles are shown with respect to the MU radar data for the following: (a) intercept and (b) slope of the least-squares regression, (c) RMSE and (d) index of agreement,  $\langle i \rangle d / i$ , for (top) the zonal wind component and (bottom) the meridional wind component. Red lines are for the JRA25 data. Yellow lines are for the ERA40 data. Orange lines are for the ERA-Interim data. Blue lines are for the NCEP1 data, and light blue lines are for NCEP2. Reanalysis data were interpolated to hourly data with MU radar height levels using the cubic spline method. Solid lines are for results with the MU radar data remaining after the first process of screening, while dashed lines in the top panels are for the zonal wind from MU radar data remaining after the first and second processes of screening. The correspondence between pressure levels and height levels follows the annual mean relationship between pressure levels and geopotential heights based on reanalysis data. See text for details.

vertical resolution of 1 km by calculating a running average of the 1 min data around each hour and around each height level. However, we found that there were still outlier data remaining after the first process, which were probably caused by ground clutter echoes, as described in the followings. In this section, we remove these data by using reanalysis data.

[54] First, we compare the winds between MU radar data and reanalysis data. 6-hourly reanalysis data are interpolated to hourly data with a vertical resolution of 1 km using the cubic spline method. We then calculate the intercept,  $a$ , and the slope,  $b$ , of the least squares regression,  $P_i = a + bO_i$ , at each height level, where  $O_i$  is a MU radar value;  $P_i$  is a reanalysis value at the grid point closest to the MU radar station, and  $i$  represents each observation time. The root-mean-square errors (RMSEs) and the index of agreement,  $d$ , are also calculated for each height level. The term  $d$  is defined as,

$$d = 1 - \left[ \frac{\sum_{i=1}^N (P_i - O_i)^2}{\sum_{i=1}^N (|P_i - \bar{O}| + |O_i - \bar{O}|)^2} \right], \quad (\text{A5})$$

where  $\bar{O}$  represents the average of  $O_i$ , and  $N$  is the total number of data used for the calculation. The index  $d$  varied from 0.0 (i.e., no agreement between  $P_i$  and  $O_i$ ) to 1.0 (i.e., perfect agreement) (see *Willmott* [1982] and SF10b for details).

[55] Figure A1 shows the vertical profiles of  $a$ ,  $b$ , RMSE, and  $d$  for zonal and meridional winds. The value of  $a$  is positive ( $1.0$  to  $3.0 \text{ m s}^{-1}$ ) for  $u$ , while it is close to zero ( $< 0.5 \text{ m s}^{-1}$ ) for  $v$ . The value of  $b$  is  $0.7$  to  $0.8$  below  $\sim 5$  km and approaches  $1.0$  with increased height. It is almost constant as  $\sim 1.0$  at  $10$  to  $15$  km and decreased with height above  $\sim 15$  km. The RMSE is larger for  $u$  ( $\sim 5.0 \text{ m s}^{-1}$ ) than for  $v$  ( $3.0 \text{ m s}^{-1}$ ). Finally,  $d$  is almost constant at  $0.9$  to  $1.0$  below  $\sim 15$  km, and it decreases with heights above  $\sim 15$  km. As pointed out by SF10b, there is no marked difference in  $d$  between zonal and meridional winds.

[56] It should be noted that these four variables indicate that the reproducibility of zonal winds is relatively worse at  $10$ – $20$  km, compared with that above and below this level;  $a$  is large ( $\sim 5.0 \text{ m s}^{-1}$ );  $b$  deviates from  $1.0$ ; the RMSE is large ( $\sim 7.5 \text{ m s}^{-1}$ ), and  $d$  is small ( $\sim 0.93$ ). It is observed that, for this height range, there are many cases in which the zonal velocities from the MU radar data are considerably smaller

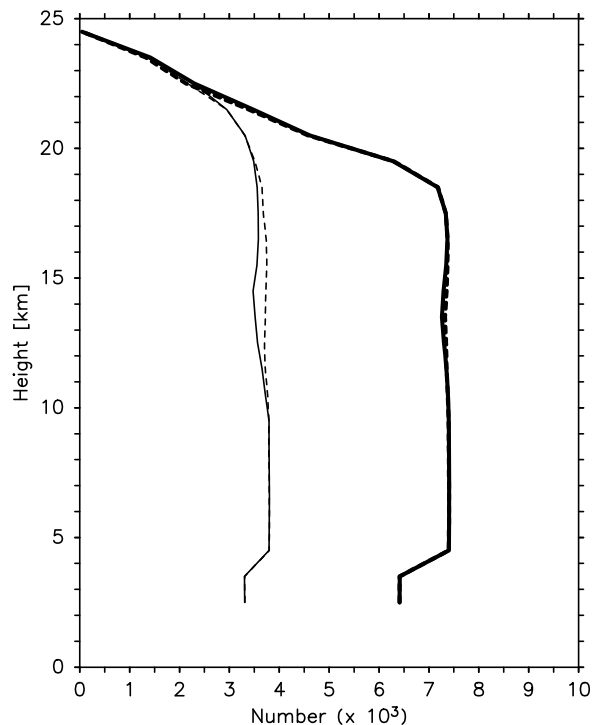


**Figure A2.** Vertical profiles of the number of valid MU radar data used for analysis. The thin and thick curves are for December through February (DJF) and June through August (JJA), respectively. The solid and dashed curves are for the zonal and meridional winds, respectively.

than those from the reanalysis data (data not shown). These data are regarded as outliers that are possibly caused by clutter echoes, which are dominant at heights (10–20 km) where the backscattered signals from the atmosphere are weak. Therefore, for the zonal wind data at 10–20 km, we only use data satisfying the condition that  $|P_i - (bO_i + a)| \leq 15 \text{ (m s}^{-1}\text{)}$ .

[57] In this paper, we use only the hourly data that are judged as valid by the above two screening processes. The results from the MU radar are produced using JRA25 data for the second process of screening ( $P_i$ ). Figure A1 also shows the vertical profiles of  $a$ ,  $b$ , RMSE and  $d$ , which are calculated using the data remaining after the two screening processes (for zonal winds). It is determined that, after the screening, the reproducibility around the tropopause improved for zonal winds. Furthermore, among the data sets, JRA25, ERA-Interim and ERA-40 performed better than NCEP1 and NCEP2 when reproducing MU radar-generated winds:  $a$  is closer to zero;  $b$  is closer to unity; the RMSE is smaller, and  $d$  is closer to unity.

[58] Figure A2 shows the vertical profiles of the hourly MU radar data used for analysis. Below ~20 km, the total number of valid data is  $\sim 4 (7) \times 10^3$ , which corresponds to ~170 days (~290 days), in DJF (JJA). The number rapidly decreases with heights above 20 km.

[59] **Acknowledgments.** The MU radar belongs to and is operated by the Research Institute for Sustainable Humanosphere (RISH) of Kyoto University. The JRA25/JCDAS data were provided by the JMA and the CRIEPI. The ERA-Interim data were obtained from the ECMWF Data Server, and NCEP reanalysis data were provided by NOAA/OAR/ESRL

PSD (Boulder, Colorado) and accessed from their Web site at <http://www.cdc.noaa.gov/>. Radiosonde data were provided by the Japan Meteorological Agency (JMA), and the GSWM00 and GSWM02 data were supplied by Maura Hagan through the Web site <http://www.hao.ucar.edu/public/research/tiso/gswm/gswm.html>. This work was supported in part by the JSC-S Scholarship Foundation and by the Japanese Ministry of Education, Culture, Sports, Science and Technology (MEXT) through Grants-in-Aid for JSPS Fellows (22002958). We are grateful to Toshitaka Tsuda, Maura Hagan, and Christopher Williams for helpful discussions and suggestions. We also thank Keiichi Ishioka, Takeshi Horinouchi, and Ying-Wen Chen for their instruction in calculating the Hough functions. We also thank three anonymous reviewers for their valuable comments on the original manuscript. All figures were drawn using the GFD-DENNOU Library.

## References

- Chapman, S., and R. S. Lindzen (1970), *Atmospheric Tides*, 200 pp., D. Reidel, New York.
- Dai, A., and J. Wang (1999) Diurnal and semidiurnal tides in global surface pressure fields, *J. Atmos. Sci.*, *56*, 3874–3891.
- Eady, E. T. (1949), Long waves and cyclonic waves, *Tellus*, *1*, 33–52.
- Forbes, J. M., and D. Wu (2006), Solar tides as revealed by measurements of mesosphere temperature by the MLS experiment on UARS, *J. Atmos. Sci.*, *63*, 1776–1797.
- Forbes, J. M., M. E. Hagan, X. Zhang, and K. Hamilton (1997), Upper atmosphere tidal oscillations due to latent heat release in the tropical troposphere, *Ann. Geophys.*, *15*, 1165–1175.
- Forbes, J. M., J. Russell, S. Miyahara, X. Zhang, S. Palo, M. Mlynarczyk, C. J. Mertens, and M. E. Hagan (2006), Troposphere-thermosphere tidal coupling as measured by the SABER instrument on TIMED during July–September 2002, *J. Geophys. Res.*, *111*, A10S06, doi:10.1029/2005JA011492.
- Fujiwara, M., et al. (2009), Cirrus observations in the tropical tropopause layer over the western Pacific, *J. Geophys. Res.*, *114*, D09304, doi:10.1029/2008JD011040.
- Fukao, S. (2007), Recent advances in atmospheric radar study, *J. Meteorol. Soc. Jpn.*, *85B*, 215–239.
- Fukao, S., T. Sato, T. Tsuda, S. Kato, K. Wakasugi, and T. Makihiro (1985), The MU radar with an active phased array system: 1. Antenna and power amplifiers, *Radio Sci.*, *20*, 1155–1168.
- Hagan, M. E., and J. M. Forbes (2002), Migrating and nonmigrating diurnal tides in the middle and upper atmosphere excited by tropospheric latent heat release, *J. Geophys. Res.*, *107*(D24), 4754, doi:10.1029/2001JD001236.
- Hagan, M. E., and J. M. Forbes (2003), Migrating and nonmigrating semidiurnal tides in the upper atmosphere excited by tropospheric latent heat release, *J. Geophys. Res.*, *108*(A2), 1062, doi:10.1029/2002JA009466.
- Hagan, M. E., J. M. Forbes, and F. Vial (1995), On modeling migrating solar tides, *Geophys. Res. Lett.*, *22*, 893–896.
- Hagan, M. E., M. D. Burrage, J. M. Forbes, J. Hackney, W. J. Randel, and X. Zhang (1999), GSWM-98: Results for migrating solar tides, *J. Geophys. Res.*, *104*(A4), 6813–6827.
- Haurwitz, B., and A. D. Cowley (1973), The diurnal and semidiurnal barometric oscillations, global distribution and annual variation, *Pure Appl. Geophys.*, *102*, 193–222.
- Held, I. M. (1983), Stationary and quasi-stationary eddies in the extratropical tropopause: Theory, in *Large-Scale Dynamical Processes in the Atmosphere*, edited by B. J. Hoskins and R. Pearce, pp. 127–168, Academic, San Diego, Calif.
- Hsu, H.-H., and B. J. Hoskins (1989), Tidal fluctuations as seen in ECMWF data, *Q. J. R. Meteorol. Soc.*, *115*, 247–264.
- Huang, C. M., S. D. Zhang, and F. Yi (2009), Intensive radiosonde observations of the diurnal tide and planetary waves in the lower atmosphere over Yichang (111°18'E, 30°42'N), China, *Ann. Geophys.*, *27*, 1079–1095.
- Huang, F. T., and C. A. Reber (2004), Non-migrating semidiurnal and diurnal tides at 95 km based on wind measurements from the High Resolution Doppler Imager on UARS, *J. Geophys. Res.*, *109*, D10110, doi:10.1029/2003JD004442.
- Kalnay, E., et al. (1996), The NCEP/NCAR 40-year reanalysis project, *Bull. Am. Meteorol. Soc.*, *77*, 437–471.
- Kanamitsu, M., W. Ebisuzaki, J. Woollen, S.-K. Yang, J. J. Hnilo, M. Fiorino, and G. L. Potter (2002), NCEP-DEO AMIP-II reanalysis (R-2), *Bull. Am. Meteorol. Soc.*, *83*, 1631–1643.
- Kodama, Y.-M., K. Egawa, and M. Takahashi (2008), Medium-scale tropopausal waves visualized by upper-level clouds to the east of Tibetan Plateau, *J. Meteorol. Soc. Jpn.*, *86*, 279–295.
- Lieberman, R. S. (1991), Nonmigrating diurnal tides in the equatorial middle atmosphere, *J. Atmos. Sci.*, *48*, 1112–1123.
- Oberheide, J., Q. Wu, T. L. Kileen, M. E. Hagan, and R. G. Roble (2006), Diurnal nonmigrating tides from TIMED Doppler Interferometer wind

- data: Monthly climatologies and seasonal variations, *J. Geophys. Res.*, *111*, A10S03, doi:10.1029/2005JA011491.
- Onogi, K., et al. (2007), The JRA-25 reanalysis, *J. Meteorol. Soc. Jpn.*, *85*, 369–432.
- Ray, R. D., and R. M. Ponte (2003), Barometric tides from ECMWF operational analyses, *Ann. Geophys.*, *21*, 1897–1910.
- Sakazaki, T., and M. Fujiwara (2008), Diurnal variations in summertime surface wind upon Japanese plains: Hodograph rotation and its dynamics, *J. Meteorol. Soc. Jpn.*, *86*, 787–803.
- Sakazaki, T., and M. Fujiwara (2010a), Diurnal variations in lower-tropospheric wind over Japan. Part I: Observational results using the Wind Profiler Network and Data Acquisition System (WINDAS), *J. Meteorol. Soc. Jpn.*, *88*, 325–347.
- Sakazaki, T., and M. Fujiwara (2010b), Diurnal variations in lower-tropospheric wind over Japan. Part II: Analysis of Japan Meteorological Agency mesoscale analysis data and four global reanalysis data sets, *J. Meteorol. Soc. Jpn.*, *88*, 349–372.
- Salby, M. L., and R. R. Garcia (1987), Transient response to localized episodic heating in the tropics. Part I: Excitation and short-time, near-field response, *J. Atmos. Sci.*, *44*, 458–498.
- Sato, K., H. Eito, and I. Hirota (1993), Medium-scale travelling waves in the extra-tropical upper troposphere, *J. Meteorol. Soc. Jpn.*, *71*, 427–436.
- Sato, K., K. Yamada, and I. Hirota (2000), Global characteristics of medium-scale tropopausal waves observed in ECMWF operational data, *Mon. Weather Rev.*, *128*, 3808–3823.
- Seidel, D. J., M. Free, and J. Wang (2005), Diurnal cycle of upper-air temperature estimated from radiosondes, *J. Geophys. Res.*, *110*, D09102, doi:10.1029/2004JD005526.
- Talaat, E. R., and R. S. Lieberman (1999), Nonmigrating diurnal tides in mesospheric and lower thermospheric winds and temperatures, *J. Atmos. Sci.*, *56*, 4073–4087.
- Tokioka, T., and I. Yagai (1987), Atmospheric tides appearing in a global atmospheric general circulation model, *J. Meteorol. Soc. Jpn.*, *65*, 423–437.
- Tomikawa, Y., K. Sato, and T. G. Shepherd (2006), A diagnostic study of waves on the tropopause, *J. Atmos. Sci.*, *63*, 3315–3332.
- Uppala, S. M., et al. (2002), The ERA-40 re-analysis, *Q. J. R. Meteorol. Soc.*, *131*, 2961–3012.
- Uppala, S. M., D. Dee, S. Kobayashi, P. Berrisford, and A. Simmons (2008), Towards a climate data assimilation system: Status update of ERA-Interim, *ECMWF Newsl.*, *115*, 12–18.
- Wallace, J. M., and F. R. Hartranft (1969), Diurnal wind variations, surface to 30 kilometers, *Mon. Weather Rev.*, *97*, 446–455.
- Wallace, J. M., and R. F. Tadd (1974), Some further results concerning the vertical structure of atmospheric tidal motions within the lowest 30 kilometers, *Mon. Weather Rev.*, *102*, 795–803.
- Whiteman, C. D., and X. Bian (1996), Solar semidiurnal tides in the troposphere: Detection by radar profilers, *Bull. Am. Meteorol. Soc.*, *77*, 529–542.
- Williams, C. R., and S. K. Avery (1996), Diurnal nonmigrating tidal oscillations forced by deep convective clouds, *J. Geophys. Res.*, *101*(D2), 4079–4091.
- Willmott, C. J. (1982), Some comments on the evaluation of model performance, *Bull. Am. Meteorol. Soc.*, *63*, 1309–1313.
- Woolnough, S. J., J. M. Slingo, and B. J. Hoskins (2004), The diurnal cycle of convection and atmospheric tides in an aquaplanet GCM, *J. Atmos. Sci.*, *61*, 2559–2573.
- Yoshida, A., and I. Hirota (1979), Diurnal wind variations in the troposphere and lower stratosphere over Japan, *J. Meteorol. Soc. Jpn.*, *57*, 29–38.
- Zeng, Z., W. Randel, S. Sokolovskiy, C. Deser, Y.-H. Kuo, M. Hagan, J. Du, and W. Ward (2008), Detection of migrating diurnal tide in the tropical upper troposphere and lower stratosphere using the Challenging Minisatellite Payload radio occultation data, *J. Geophys. Res.*, *113*, D03102, doi:10.1029/2007JD008725.
- Zhang, X., J. M. Forbes, M. E. Hagan, J. M. Russell III, S. E. Palo, C. J. Mertens, and M. G. Mlynczak (2006), Monthly tidal temperatures 20–120 km from TIMED/SABER, *J. Geophys. Res.*, *111*, A10S08, doi:10.1029/2005JA011504.

M. Fujiwara and T. Sakazaki, Graduate School of Environmental Science, Hokkaido University, N10 W5, Sapporo 060-0810, Japan. (zaki@ees.hokudai.ac.jp)

H. Hashiguchi, Research Institute for Sustainable Humanosphere, Kyoto University, Gokasho, Uji 611-0011, Japan.